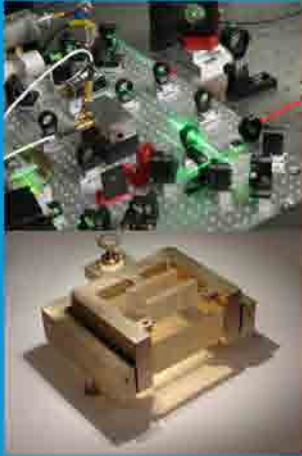
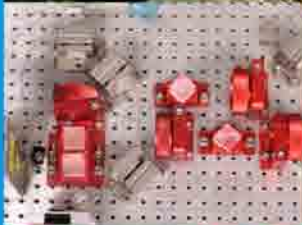


institute for optical systems



institut für optische systeme | konstanz
ios >
optische messtechnik | bildverarbeitung | bildtechnik

annual report 2009



ios konstanz
htwg konstanz
brauneggerstr. 55
78462 konstanz
www.ios.htwg-konstanz.de

Foreword



Institute for Optical Systems IOS - one of the HTWG key research institutes

The HTWG Konstanz started in 2007 an intensive internal discussion on defining key topics that should be supported to extend the success in research and technology transfer. Criteria in the discussion at that time have been:

- Existing success and promising success in future
- Interdisciplinary
- Perceptibility
- Linked to study programs
- Interest of society and researchers to the topic

One of the key topics that have been defined led to the founding of IOS Institute for Optical Systems: Optical Technologies and Image Processing. Professors with different research emphases within this framework from different HTWG departments focussed their activities under the brand of IOS, using synergies and cooperating in applying for different public grants and private money. Their individual success and the success of the institute itself are demonstrated in the present annual report.

IOS links professors, doctoral and master students together to each other and to industry effecting results in applied research and supporting the study programs of HTWG as well.

I wish the IOS ongoing success in its wide and challenging subject.

A handwritten signature in black ink that reads "Gunter Voigt". The signature is written in a cursive, flowing style.

Prof. Dr.-Ing. Gunter Voigt
Vice-President for Research, University of Applied Sciences Konstanz

Preface

The present report gives an overview over the research and development activities of the Institute for Optical Systems (IOS) Konstanz in the year 2009. Our main fields of interest are optical metrology, image processing, computer graphics and light engineering, thus representing the fundamental disciplines of current optical technology. The focus on optical systems as a whole allows us to offer competent partnership to the local industry in all relevant aspects. The IOS was founded in April 2008 by four professors from three different faculties of the University of Applied Sciences at Konstanz and is led by Prof. Dr. Braxmaier (director) and Prof. Dr. Franz (associate director).

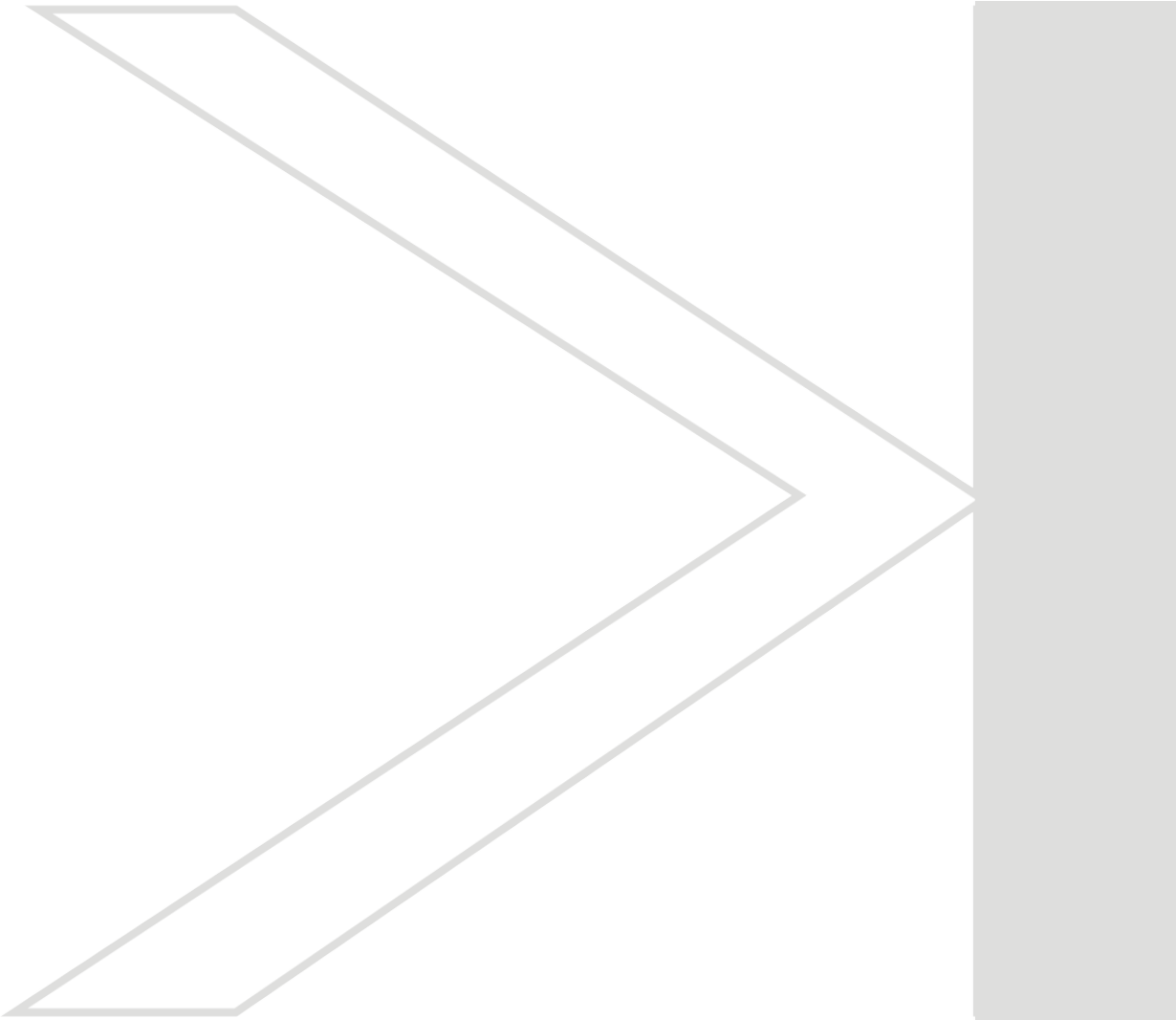
The following project descriptions present ongoing activities mainly on a status report level. Most of the reports are written by students working on their diploma, bachelor, master or Ph.D. theses. They reflect the largely varying levels of content, practice and insight that are characteristic for an institution involved in academic education. Due to its interdisciplinary nature, research at the IOS combines approaches from optics, metrology, light engineering, sensor technology, computer graphics, image and signal processing, typically resulting in optical systems on a prototype level, either in prephase research or in cooperation with local industry.

On the occasion of our second annual report, we would like to thank all of our students and co-workers for their enthusiasm and dedication which makes our still rudimentary institute a great place to be. We are also indebted to the administration and staff of the HTWG Konstanz for their help and support during this startup phase, especially president Dr. Kai Handel and Prof. Dr.-Ing. Gunter Voigt, for the support and start-up funding and the faculties of Mechanical Engineering, Electrical and Information Engineering, and Computer Science with the deans Prof. Dr.-Ing. Carsten Manz, Prof. Dr.-Ing. Werner Kleinhempel and Prof. Dr.-Ing. Oliver Bittel for their assistance. Furthermore we appreciate the support of the Institute for Applied Research (IAF) Konstanz, especially Prof. Dr. Horst Werkle and Dipl.-Ing. FH Andreas Burger.

Contents

Institute Profile	7
IOS Building and Location Plan	9
Institute Members	10
IOS Staff	11
External Fundings and Grants	11
Cooperations with Research Institutions and Industry	12
Theses and Student Projects	13
Publications	14
Laboratories	18
Research Activities	21
Picometer and Nanoradian Heterodyne Interferometry	23
Setup of an Ultra-Stable Interferometer Using Novel Integration Techniques	25
Development of RF Quadrant Photodetectors	27
Development of an Ultraprecise Digital RF Phasemeter	29
Laser Frequency Stabilization to Optical Resonators	31
Validation of In-Field Pointing Concepts for LISA	33
Investigations towards μN High Efficiency Multistage Plasma Thrusters	35
High Precision Optical Metrology	37
Measurements on Single Mode Waveguides in a Mid-Infrared Test Interferometer	39
Development of a Tilt Actuated Mirror	43
Space Time Asymmetry Research – STAR	45
High Resolution Optical Profilometry	47
3D-Digitization Using Fringe Projection and HDR Methods	49
Preparation of the ‘Fertigungs-Messtechnik 2’ Laboratory	51
The Statistics of Vegetation Echoes as Received by Echolocating Bats	53
Steganalysis Using Stochastic Image Models	55
The <i>Optical Radar</i> - a Multidisciplinary Research Project	57
A Bracket for a Rapidly Rotating Mirror	59
Calibration of the Sensor Axis	61
Removal of Complex Lens Distortions	63
Texture Continuation with Texture Synthesis and Inpainting	65
Digital Image Steganography	67
Real-Time Multi-Camera Matching for 3D Reconstruction	69
Adaptive Tetrahedral Subdivision for Finite Element Analysis	71
Optische Drehzahlmessung nach dem Korrelationsverfahren	73

Institute Profile



IOS BUILDING AND LOCATION PLAN



Institute for Optical Systems

Brauneggerstraße 55
Building E
3rd and 4th floor
78462 Konstanz



Location Plan

Prof. Dr. Claus Braxmaier:



Diploma in precision engineering at University of Applied Sciences Furtwangen. Diploma in physics and doctoral degree at the University of Konstanz in the field of fundamental tests of physics. Post-Doc at University of Konstanz. At EADS Astrium GmbH, system responsible for scientific and earth observation missions for ESA and head of group 'Mission Metrology'. Since 2005 professor for physics and control theory at the University of Applied Sciences Konstanz. Member of 'Institut für Angewandte Forschung (IAF)' and 'Institut für Naturwissenschaften und Mathematik' Konstanz. Since 2008 director of the 'Institute for Optical Systems (IOS) Konstanz'. Head of optical metrology research labs at HTWG and EADS Astrium GmbH. Main research: high resolution optical metrology for industrial and space applications.

Prof. Dr. Matthias Franz:



M.Sc. in Atmospheric Sciences from SUNY at Stony Brook, Diploma in physics from the Eberhard-Karls-Universität, Tübingen and doctoral degree in 1998. Thesis research in visual insect and robot navigation at the MPI for Biological Cybernetics and as a PostDoc at the Australian National University in Canberra. In industry he worked on various aspects of autonomous vision systems. 2002, he returned to the MPI as a group leader in the area of machine learning and computer vision. Since 2007 professor at the University of Applied Sciences in Konstanz and head of cognitive systems lab. Member of 'Institut für Angewandte Forschung (IAF)'. Main research activities in the development of automatically generated vision systems, optimisation and probabilistic modeling, with applications in industrial machine vision, texture analysis and steganalysis.

Prof. Dr. Georg Umlauf:



Diploma in computer science from University of Karlsruhe, 1996. Doctoral degree in computer science from University of Karlsruhe, 1999. PostDoc at University of Karlsruhe and University of Florida, Gainesville, USA, 1999-2000. Software development and senior researcher at Tebis AG, Hamburg, 2000-2002. Assistant professor for geometric algorithms at University of Kaiserslautern, 2002-2009. Interim professor for computer graphics at University of Karlsruhe, 2009. Since 2009 professor for computer graphics at University of Applied Sciences Konstanz and head of the computer graphics lab. Since 2010 member of the 'Institute for Optical Systems (IOS)' and 'Institute for Applied Research (IAF)'. Main research interests: Computer graphics, geometric modeling (splines, subdivision), reverse engineering, physical simulations.

Prof. Dr. Bernd Jödicke:



Study of physics at the University of Karlsruhe. Doctoral degree at Technical University Hamburg and University Karlsruhe in the field of high frequency technology. After that, industrial work at ABB Baden, Switzerland, as executive director for R&D. Since 1992 professor for applied physics at University of Applied Sciences Konstanz. Member of 'Institute for Applied Research (IAF)', 'Institut für Naturwissenschaften und Mathematik (INM)', 'Institute for Optical Systems (IOS) Konstanz' and 'Deutsche Lichttechnische Gesellschaft'. Head of laboratory for light engineering at HTWG. Main research activities in color and light measurements and color camera systems.

Prof. Dr. Klaus-Dieter Durst:



Study of physics at the University of Stuttgart, 1986 doctoral degree in the field of magnetism at the Max-Planck-Institute of metal research. Thereafter research center Weissach of the Dr. Ing. h.c. F. Porsche AG, responsible for the central unit 'measurement technologies'. Since 1993 professor for measurement engineering and sensor technology at the University of Applied Sciences Konstanz. Member of 'Institut für Naturwissenschaften und Mathematik' and 'Institute for Optical Systems' Konstanz. Head of laboratories for measurement and sensor technology and production metrology. Currently director of 'Institut für Naturwissenschaften und Mathematik' Konstanz. Activities in the accreditation and surveillance of testing laboratories and inspection bodies.

IOS STAFF

Professors	Claus Braxmaier, director IOS Matthias Franz, associate director IOS Georg Umlauf Bernd Jödicke Klaus-Dieter Durst
Officer	Ruven Spannagel
Technical Staff (INM)	Hermann Richter Karl-Heinz Waller Dietmar Merk
Academic Staff	Mohammed Allab, mechanical engineering Stefan Jacob, computer science, Breuckmann
PhD Students	Thilo Schuldt, physics Martin Gohlke, physics, EADS Astrium Andreas Keller, physics, EADS Astrium Jürgen Keppler, computer science Le Pham Hai Dang, computer science Klaus Denker, computer science Trendafil Ilchev, mechanical engineering
Student Assistants	Stefan Lang, computer science Markus Messmer, computer science
Interns	Pius Höger (BOGY)



EXTERNAL FUNDINGS AND GRANTS

- ZAFH PHOTONⁿ (European Union under EFRE and Baden-Württemberg funding); "Miniatur Lasersensor", 1 PhD student and equipment funds.
- BMBF (Federal Ministry of Education and Research) grant ("Young Engineers" funding line); "Optische 3D-Mess- und Digitalisierungssysteme für den Einsatz im Maschinenbau", 2 academic staff and equipment funds.
- BMBF (Federal Ministry of Education and Research) grant ("Young Engineers" funding line): "Detection of steganography in images using statistical models", 1 PhD student and equipment funds.
- Structure and Innovation Fund for Research, Baden-Württemberg, grant: "Automation and Communication", equipment funds.
- Baumer Inspection GmbH, Konstanz: "Inspection of surfaces", contract research.
- Medav GmbH; Ilmenau: "Detection of steganography in images using statistical models", contract research.

COOPERATIONS WITH RESEARCH INSTITUTIONS AND INDUSTRY

Academic and Institutional Cooperations

- HTW Aalen
- HFU Furtwangen
- Humboldt-Universität zu Berlin
- Stanford University, USA
- NASA AMES Research Center, USA
- KACST, King Abdulaziz City for Science and Technology, Riyadh, Kingdom of Saudi Arabia
- ZARM (drop tower), Center of Applied Space Technology and Microgravity, Bremen
- DLR Institut für Raumfahrtsysteme Bremen
- University of Tübingen
- Max-Planck-Institute for Biological Cybernetics, Tübingen
- German Federal Office for Information Security (BSI), Bonn
- Weizmann Institute of Science, Rehovot, Israel
- INCM-CNRS UMR, Marseille, France

Industry Cooperations

- EADS Astrium, Immenstaad
- Breuckmann GmbH, Meersburg
- Chromasens GmbH, Konstanz
- Medav GmbH, Ilmenau
- Baumer Inspection GmbH, Konstanz
- Procon-System GmbH, Thierstein

THESES AND STUDENT PROJECTS

Diploma Theses

- M. Schwierz, Modularer Aufbau und Charakterisierung des hochauflösenden und optischen, Sub-Nanometer-Profilometer (kurz: NANO-PRO) genannten, Messsystems mit linearer Aktorik, Diploma Thesis (2009), computer science.
- M. Jawinsky, Kolorimetrische Kalibrierung eines multispektralen Aufnahmesystems, Diploma Thesis, (2009), computer science.
- A.T. Abchir, Gaußsche Prozesse für große Datenmengen, Diploma Thesis, (2009), computer science.
- F. Andriamahandrimanana, Prädiktion von prozessorientierten Veränderungen des Farbeindrucks, Diploma Thesis, (2009), computer science.
- T. Gräß, Unüberwachte adaptive optische Oberflächenkontrolle von Möbelplatten, Diploma Thesis, (2009), computer science.
- C. Balles, Oberflächenkontrolle von beschichteten Holzfasernplatten mittels intelligenter Auflichtbeleuchtung, Diploma Thesis, (2009), computer science.
- C. Kungel, Umsetzung eines Prototypen zur robusten Fahrzeugdetektion und Fahrzeugverfolgung in Echtzeit in monokularen Verkehrssequenzen, Diploma Thesis, (2009), computer science.

Master Theses

- T. Gekeler, Umfeldkartierung mit Bildverarbeitung aus Rundum-Videosensorik für Einparkfunktion im Automobil, Master Thesis, (2009), computer science.
- I. Schiffler, Entwicklung eines IR-Spektralphotometermoduls, Master Thesis (2009), mechanical engineering.
- D. Kessler, Visualisierung der Strömungsphänomene von Öl mit definiertem Luftgehalt in Innenzahnradpumpen, Master Thesis (2009), mechanical engineering.

Bachelor Theses

- S. Ressel, Integration Technologies for Optical Components and Design of a High Precision Interferometer, Bachelor Thesis (2009), mechanical engineering.
- A. Oguz, Aufbau eines Testbeds zur Messung des relativen Intensitätsrauschens von Lasern, Bachelor Thesis (2009), electrical engineering.
- M. Maurer, Entwicklung eines Quadranten-Photodetektors zur hochgenauen Phasen- und Wellenfrontmessung bis 20 MHz, Bachelor Thesis (2009), electrical engineering.
- F. Kittelmann, Entwicklung eines FPGA-basierten ultrapräzisen RF-Phasenmeters, Bachelor Thesis (2009), information technology.
- R. Spannagel, Integration und Test der Aktorik für ein Laserinterferometer zur hochauflösenden optischen Profilometrie, Bachelor Thesis (2009), electrical engineering.
- C. Beurer, Optische 3D-Koordinatenmesstechnik mit codierter Streifenprojektion und Bildverarbeitung mit Schwerpunkt Flächenrückführung, Bachelor Thesis (2009), mechanical engineering.

Internships

- A. Pereyra, Aufbau eines optischen Metrologie-Systems zur Charakterisierung von schmalbandigen Lasersystemen für Weltraumanwendungen, Internship Report (2009), electrical engineering.
- F. Kittelmann, Implementation of a Phasemeter in a FPGA, Internship Report (2009), information technology.
- S. Waimer, Hochpräzise Bestimmung des linearen thermischen Ausdehnungskoeffizienten mittels einem hochsymmetrischen Heterodyn-Interferometers, Internship Report (2009), electrical engineering.
- D. Küsters, Hochauflösende dynamische Charakterisierung eines Walking Piezo Motors, Internship Report (2009).

Student Projects

- M. Liebhart und W. Baumgartner, Konzeption, Design und Realisierung einer Messstrahlaktuation für die höchstauflösende optische Profilometrie, Master Project (2009), mechanical engineering.
- D. P. Fink, A. F. Zillinger, Inbetriebnahme einer 3D-Koordinatenmeseinrichtung mit Bildverarbeitungssensor, Bachelor Project (2009), mechanical engineering.
- A. Resch, Schlupffreie Geschwindigkeitsmessung nach optischem Korrelationsverfahren, Master Project (2009), mechanical engineering.
- T. Pitzner, S. Voigt, Inbetriebnahme einer 3D-Mess- und Digitalisierungseinrichtung, Bachelor Project (2009), mechanical engineering.

Journal Papers

- T. Schuldt, M. Gohlke, D. Weise, U. Johann, A. Peters, and C. Braxmaier, Picometer and nanoradian optical heterodyne interferometry for translation and tilt metrology of the LISA gravitational reference sensor, *Classical and Quantum Gravity* 26 (2009).
- J. Cordero, T. Heinrich, T. Schuldt, M. Gohlke, S. Lucarelli, D. Weise, U. Johann, and C. Braxmaier, Interferometry based high-precision dilatometry for dimensional characterization of highly stable materials, *Meas. Sci. Technol.* 20 (2009).
- T. Schuldt, M. Gohlke, R. Spannagel, S. Ressel, D. Weise, U. Johann, and C. Braxmaier, Sub-Nanometer heterodyne Interferometry and its Application in Dilatometry and Industrial Metrology, *Int. J. Opt. Mech.* 3, 187 – 200 (2009).
- H. Schneckenburger, R. Börret, C. Braxmaier, R. Kessler, P. Kioschis, D. Kühlke, U. Mescheder, W. Schröder und C. Nachtigall, Dem Energiestoffwechsel von Tumorzellen und Bioreagenzien auf der Spur, *BioPhotonik*, 26 – 28, (September 2009).
- Y. Yovel, P. Stilz, M.O. Franz, A. Boonman, H.-U. Schnitzler, What a Plant Sounds Like: The Statistics of Vegetation Echoes as Received by Echolocating Bats. *PLoS Comput. Biol.* 5(7): e1000429. doi:10.1371/journal.pcbi.1000429 (2009).
- Y. Yovel, M.L. Melcon, M.O. Franz, A. Denzinger, H.-U. Schnitzler, The Voice of Bats: How Greater Mouse-eared Bats Recognize Individuals Based on Their Echolocation Calls. *PLoS Comput. Biol.* 5(6): e1000400. doi:10.1371/journal.pcbi.1000400 (2009).
- W. Kienzle, M.O. Franz, B. Schölkopf, F.A. Wichmann, Center-surround patterns emerge as optimal predictors for human saccade targets. *Journal of Vision*, 9(5):7, 1-15, <http://journalofvision.org/9/5/7/>, doi:10.1167/9.5.7 (2009).
- T. Bobach, G. Farin, D. Hansford, G. Umlauf: Natural neighbor interpolation using ghost points, *Computer Aided-Design*, 41(5): 350-365 (2009).

Peer Reviewed Papers in Conference Proceedings

- M. Gohlke, T. Schuldt, D. Weise, U. Johann, A. Peters, and C. Braxmaier, A high sensitivity heterodyne interferometer as a possible optical readout for the LISA gravitational reference sensor and its application to technology verification, in: *Journal of Physics: Conference Series* 154 - Proceedings of the 7th International LISA Symposium (2009).
- M. Gohlke, T. Schuldt, D. Weise, U. Johann, A. Peters, and C. Braxmaier, Development of an ultrasensitive interferometry system as a key to precision metrology applications, *Proc. SPIE Vol. 7389, 73890V* (2009). SPIE Europe – Optical Metrology, Munich.
- T. Schuldt, M. Gohlke, R. Spannagel, S. Ressel, D. Weise, A. Peters, U. Johann, and C. Braxmaier, High-resolution dimensional metrology for industrial applications, *Proc. of ISMTII*, (2009). ISMTII, St. Petersburg.

- M. Gohlke, T. Schuldt, D. Weise, A. Peters, U. Johann, and C. Braxmaier, A High Precision Heterodyne Interferometer for Relative and Absolute Displacement Measurement, IEEE Conference Proc. ISOT (2009). ISOT, Istanbul.
- T. Schuldt, M. Gohlke, D. Weise, U. Johann, and C. Braxmaier, A high-precision dilatometer based on sub-nm heterodyne interferometry, IEEE Conference Proc. ISOT (2009). ISOT, Istanbul.
- A. Barbero, M.O. Franz, W. v. Drongelen, J.R. Dorronsoro, B. Schölkopf, M. Grosse-Wentrup, Implicit Wiener Series Analysis of Epileptic Seizure Recordings, Proc. 31st Annual International Conference of the IEEE Engineering in Medicine and Biology Society (EMBC'09), Minneapolis, MN, USA, 5304-5307, 2009.

Conference Talks (without Proceedings)

- M. Gohlke, T. Schuldt, D. Weise, U. Johann, A. Peters, and C. Braxmaier, A High Resolution Interferometer for LISA and its Application to Technology Verification, DPG – Frühjahrstagung, Hamburg (2009).
- S. Waimer, M. Gohlke, D. Weise, T. Schuldt, U. Johann, A. Peters, and C. Braxmaier, Ein optisches Dilatometer zur hochpräzisen CTE-Wert Bestimmung, DPG – Frühjahrstagung Hamburg (2009).
- T. Schuldt, M. Gohlke, D. Weise, U. Johann, A. Peters, and C. Braxmaier, Picometer and Nanoradian Interferometry for the LISA Gravitational Reference Sensor and its Application to Technology Verification, CLEO Europe, Munich (2009).
- K. Denker, G. Umlauf, Real-time triangulation of point streams, SIAM Conference on Mathematics for Industry: Challenges and Frontiers, San Francisco, USA (2009).
- D. Burkhart, G. Umlauf, An adaptive tetrahedral subdivision scheme for finite element analysis, SIAM/ACM joint Conference on Geometrical and Physical Modelling, San Francisco, USA (2009).
- G. Umlauf, Real-time triangulation of point streams, SIAM/ACM joint Conference on Geometrical and Physical Modelling, San Francisco, USA (2009).
- G. Umlauf, Adaptive tetrahedral subdivision for FEM simulations, Workshop: Subdivision and Refinability, Pontignano, Italien (2009).
- G. Umlauf: Real-time triangulation of point streams, Symposium Geometric modelling, visualization and image processing, FH Stuttgart (2009).
- G. Umlauf, Online triangulation of laser scan data, Workshop Industry challenges in geometric modelling, CAD and simulation, TU Darmstadt (2009).
- B. Jödicke, Baumgartner, Drotleff, Hellbrück, et.al: Einfluss und Wechselwirkung von dynamischem Licht und Akustik auf die Leistungsfähigkeit von Mitarbeitern, 14. Symposium Licht und Architektur; Staffelstein (02/2009).

Papers, not Reviewed

- B. Jödicke, Büroeffizienz. Das Projekt und die Ziele, Züblin, Stuttgart (Dezember 2009).

Awards

- K. Denker, Nachwuchspreis des Bezirksverbandes Pfalz, Kaiserslautern, 07.11.2009, Preisgeld 5000€.

Selected Media Coverage

- BBC: <http://news.bbc.co.uk/2/hi/science/nature/8085477.stm>, voice recognition in bats
- Tehran Times: http://www.tehrantimes.com/index_View.asp?code=196162, voice recognition in bats
- Ynet: <http://www.ynet.co.il/articles/0,7340,L-3732275,00.html>, voice recognition in bats
- Focus online: http://www.focus.de/finanzen/karriere/berufsleben/arbeitsplatz/arbeitsplatz-suche-nach-dem-wohlfuehl-buero_aid_380761.html Das Wohlfühlbüro, Das Wohlfühlbüro
- Esslinger Zeitung: Das Wohlfühlbüro
- Main Post: Das Wohlfühlbüro
- Interview Radio Hamburg: Das optimale Büro der Zukunft



LET – Laboratory for Enabling Technologies

The Laboratory for Enabling Technologies (LET) was founded in 2007 at Astrium Friedrichshafen within the department Science Missions & Systems (AED41, head: Dr. Ulrich Johann). It is managed in close collaboration with the optical metrology group of Prof. Braxmaier of the IOS Konstanz and devoted to research and development of novel technologies crucial to the success of future space missions and systems. Led by Prof. Claus Braxmaier (HTWG) and Dr. Dennis Weise (Astrium), the LET provides the framework for student projects carried out in PhD., master and bachelor theses as well as internships where the main fields of studies are mechanical engineering, electrical engineering, information technology/computer science and physics. The highly-motivating atmosphere together with interdisciplinary leading-edge space re-

search attracted numerous students over the past years. The direct interaction with the scientific community is considered as a key success factor for the LET effectiveness.

The LET comprises state of the art optical lab equipment, including vibration isolated optical tables, frequency and wavelength analysis and laser systems (including an iodine stabilized reference laser).

Current activities include the development of following key technologies for future space missions:

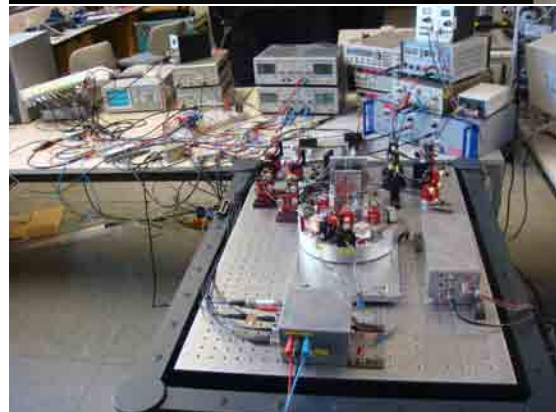
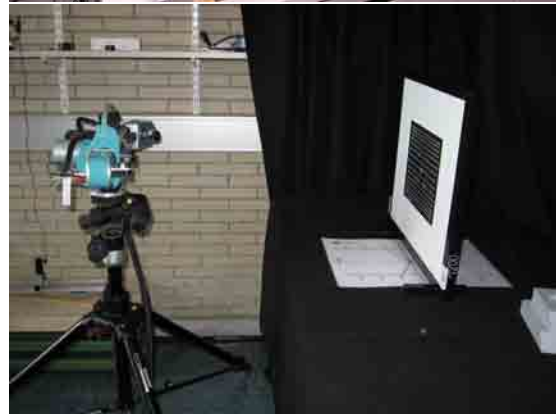
- Space laser metrology for inertial sensors
- AI technology for optical systems
- μN thrusters
- Actuators for space applications
- Frequency references
- Test beds for future missions

Laboratory for Applied Optics

The laboratory for applied optics is located in building G of HTWG and is led by Prof. Claus Braxmaier. On the one hand, this lab includes research activities of the IOS in the field of applied optics (which are also detailed in the research activities descriptions), on the other hand this lab represents the basis for optical experiments carried out by students during different study programs. Several fundamental optical experiments are build up for student education, including

- Optical profilometry
- Actuators for beam manipulation
- Interferometry (Michelson, Mach-Zehnder)
- Optical data transmission
- 3D optical digitalization using fringe method
- Fizeau interferometry for topography
- Triangulation measurement
- Basic optical experiments (e.g. diffraction, dispersion)

Several bachelor, master and diploma thesis as well as student projects were carried out in the laboratory for applied optics. This includes students from different faculties such as Mechanical Engineering, Electrical Engineering and Information Technology, Computer Sciences.



Computing Infrastructure



The compute and network environment of the institute is based on Intel and AMD multicore architectures connected with 1 GBit Ethernet. The 20 workstations use the operating systems Ubuntu Linux, Microsoft Windows and Mac OS. The central file server is integrated in the cluster system. For computation-intensive applications, such as multispectral image processing or the training of learning machines, we run a compute cluster under Ubuntu Linux. The cluster consists of a master node and a compute node with Intel Xeon CPUs, providing 40 processor kernels and 256 GB of RAM. Both nodes are mounted in a liquid-cooled rack with a 10 kW UPS. The internal cluster communication uses 2 GBit Ethernet and connects via FibreChannel to a RAID 6 storage system with 3.5 TB capacity to guarantee a high data throughput. Resources are managed with the SUN GridEngine. The cluster is connected to the backbone of the HTWG network via 10 GBit FibreChannel. Data backup is guaranteed by the central computer services of the HTWG.

Image Sensor Laboratory



The Image Sensor Laboratory is used to build, evaluate and calibrate the various camera systems used in the image processing projects of the IOS. Preliminary experiments are run directly in the IOS main office in a laboratory section which can be isolated with a light-proof curtain, whereas higher precision experiments are done in various laboratories on the HTWG campus with appropriate facilities. For high-resolution multispectral imaging, we dispose of a Peltier-cooled pco.4000 14 bit camera with a 4008×2672 CCD array and a VariSpec Tunable Filter that allows for selecting an arbitrary 30 nm wide band in the visual range via a computer interface. For inspecting and processing colour images, we use a specialised graphics workstation with a high-fidelity calibrated colour display. Spectral measurements are done with a KonicaMinolta CS 2000 absolute spectrometer. In applications requiring high CCD sensor sensitivities (such as the optical radar project), we have another Peltier-cooled pco.1600 colour camera with less resolution, but higher sensitivity.

Research Activities



Picometer and Nanoradian Heterodyne Interferometry

Martin Gohlke, Thilo Schuldt, Achim Peters, Ulrich Johann, Dennis Weise, and Claus Braxmaier



We present a symmetric heterodyne interferometer as prototype of a highly sensitive translation and tilt measurement system. It was developed as possible candidate for the optical readout aboard the LISA (Laser Interferometer Space Antenna) satellites and becomes the key technology for LISA related performance tests during the last years, for example: expansion measurements in a dilatometer or high precision measurements of piezo actuators and mechanisms. We show the current performance of the interferometer and the results of the performed noise studies in 2009.

Introduction

The planned LISA Mission aims to detect gravitational waves in the frequency band from 1 mHz to 1 Hz [1]. Gravitational waves stretch and shrink the space-time – consequently a typical gravitational wave causes a small change of the distance L between two proof masses, i.e. $\Delta L/L \approx 10^{-21}$. In the LISA concept, three satellites – a free falling proof mass aboard of each – are forming an equilateral triangle with an edge length of around 5 million km. The edge length changes about few pm (10^{-12} meter) when a gravitation wave passes. This leads to the requirements for the positioning sensors aboard the satellites:

- translation measurement noise

$$< 1 \text{ pm} \times \sqrt{1 + \left(\frac{2.8 \text{ mHz}}{f}\right)^4}$$
- measurement of the proof mass tilt
- low interaction with the proof mass
- measurement band from 1 mHz to 1 Hz

An optical readout (ORO) is the current baseline in the LISA concept.

EADS Astrium (Friedrichshafen), in collaboration with the Humboldt University Berlin and HTWG Konstanz, has realized a prototype ORO

over the past years. The heterodyne interferometer [2] is based on a highly symmetric design where both, measurement and reference beam have a similar optical pathlength and the same frequency and polarization. The technique of differential wavefront sensing (DWS) for tilt measurement is implemented. With this setup noise levels below $5 \text{ pm Hz}^{-1/2}$ for translation and below $10 \text{ nrad Hz}^{-1/2}$ for tilt measurements – both for frequencies above 10 mHz – were demonstrated. With this excellent noise performance the interferometer is a useful tool for many applications in the LISA context and other concept studies.

In 2009 we investigated noise sources of the existing setup, especially the phasemeter, the analog-digital converters (ADCs) and the front-end electronics (photo diodes). Beside these "noise hunting" activities we also plan a new interferometer setup. The baseplate will be made of Zerodur, an ultra stable glass ceramic with a low coefficient of thermal expansion ($\text{CTE} \approx 0.02 \cdot 10^{-6} \text{ K}^{-1}$) instead of aluminum as in the current setup.

Current Status

The interferometer setup can be divided into four parts: laser, optical setup, front-end electronics and phasemeter. In 2009 we have investigated the noise

sources starting at the phasemeter.

Our digital phasemeter is implemented on a field programmable gate array (FPGA) board. The eight incoming analog signals are converted by 16-bit analog-digital converters at 160 kHz. Each digitized signal is mixed with an internal 10 kHz sinusoidal signal, the product passes a low-pass filter. Afterward the phase-containing signal can be stored in FIFO (first-in-first-out) memory. The FIFO information is used by a LabView program to compute translation and tilt of the proof mass.

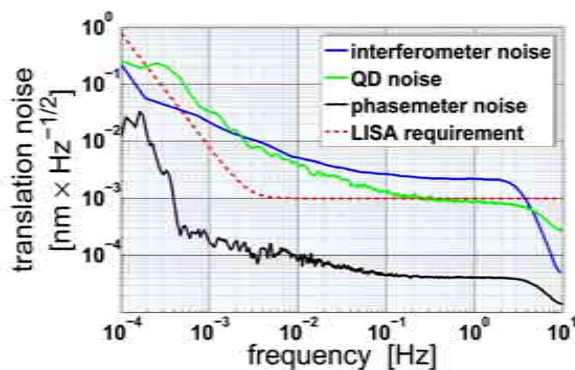


Figure 1: Root of the power spectrum density of different time series noise measurements. The red (dashed) line corresponds to the LISA requirement. The lowest (black) line represents the phasemeter noise, the middle (green) line stands for the noise contributions of the photodiodes and the upper (blue) line is the current interferometer performance.

In a first step we analyzed the noise and the sampling-time delay (cf. 2) of all eighth ADCs on the FPGA board. As result, their influence onto the measurement performance is negligible. In a second step a "pure" interferometer signal was simulated by use of a function generator in combination with a power divider. The divided signals were the inputs for the phasemeter. The root of the power spectrum density ($PSD^{1/2}$) of this test is depicted in figure 1 (black line). With a noise level of 40 fm at higher frequencies the phasemeter is not the limiting factor of the interferometer setup.

In a next step we investigated the influence of the front-end electronics. Therefore we built an optical setup where reference and measurement beam were represented by the same optical input signal. The measured noise performance is de-

scribed in figure 1 as green line. The noise performance seems to be better than the interferometer performance, but the signal levels were different. Therefore, we believe that we are currently limited by the noise of the photodiodes.

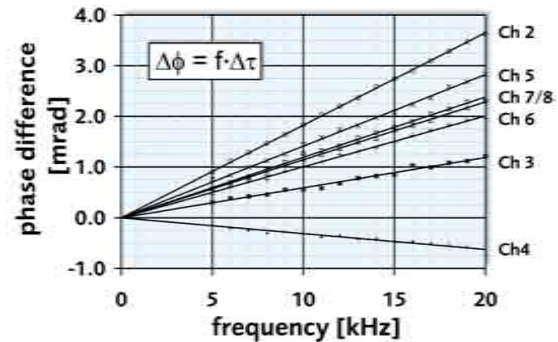


Figure 2: ADC-delay measurement. The relative delays between channel 1 and the other seven input channels lead to a phase shift (linearly dependent) between the incoming signals.

Next Steps

Currently new low-noise photodiodes are tested under the same conditions as in the test described above. With these photodiodes it also will be possible to change the beat frequency from 10 kHz to 2 – 20 MHz which is currently baseline in the LISA concept. For phase measurements at this higher frequency range a new phasemeter is developed. The main goal for 2010 is the integration of a new Zerodur-based interferometer using adhesive bonding as integration technology.

Bibliography

- [1] P. Bender et al. Pre-Phase A Report, Second Edition, 1998
- [2] T. Schuldt, M. Gohlke, D. Weise, U. Johann, A. Peters, C. Braxmaier: Picometer and nanoradian optical heterodyne interferometry for translation and tilt metrology of the LISA gravitational reference sensor, *Class. Quantum Grav.* 26, 2009.

Setup of an Ultra-Stable Interferometer Using Novel Integration Techniques

Thorsten Meisner, Scarlett Strohmaier, Simon Ressel, Dominik Rauen, Martin Gohlke, Ulrich Johann, Dennis Weise, and Claus Braxmaier



A new high-sensitivity and ultra-stable heterodyne-interferometer is developed which is an advanced version of an already existing system. With help of special integration techniques the interferometer setup realized on an aluminum base plate will be transferred to a baseplate made of Zerodur. The aim is to measure resolutions on picometer and nanoradian level fulfilling the LISA requirements concerning acceptable noise levels. In particular it is assumed that thermal noise will be reduced because Zerodur shows a very low coefficient of thermal expansion and is therewith qualified to withstand high temperature gradients. Further effort is the miniaturization of the existing system. In this report the design and the integration technique is described.

Based on the experience with our high sensitivity heterodyne interferometer, an advanced interferometer setup is developed where the baseplate is made of Zerodur, a glass ceramics with a very low coefficient of thermal expansion of $2 \cdot 10^{-8} \text{ K}^{-1}$. The optical components are made of fused silica and fixed to the baseplate using adhesive bonding technology. In this report we describe the integration technology, the design of the new interferometer and the development of specific adjustment tools needed for interferometer integration.

Integration technology

The methods of adhesive bonding and hydroxide-catalysis bonding were evaluated with respect to fixing the optical components to the Zerodur baseplate. A testboard with 6 mirrors fixed to a baseplate made of Zerodur using both integration techniques was set up and vibration and shock tests were carried out in the Vibration Test Facilities of EADS Astrium in Friedrichshafen. While the vibration tests were realised with a sine and a random stimulation, the shock tests were performed according the ECSS and the LISA Pathfinder requirements. A temperature cycling stability was also carried out. The testboard was placed in a thermal

chamber and according to the LISA requirements the temperature range was controlled from -20°C to 50°C . This range was cycled eight times during 51 hours with a temperature change rate of $2^{\circ}\text{C}/\text{min}$. Before and after these tests the alignment of the mirrors concerning their angles to each other was measured. The measured deviations lay within the measurement error bars. In both investigations, no appreciable disadvantage of one of the two bonding methods could be observed. However, for the design of the new interferometer it is decided to use the method of adhesive bonding. For the integration of the optical components on Zerodur it is advisable to have enough time to align the components if applicable. Since a broader time frame and lower requirements of space-qualified adhesives, adhesive bonding is more feasible.

Design of the new interferometer

The new heterodyne interferometer was planned with the CAD software Autodesk Inventor. The beam path of the new interferometer is shown in figure 1 (top), it is placed on a breadboard with the dimensions $200 \times 200 \times 40 \text{ mm}^3$ ($l \times w \times h$).

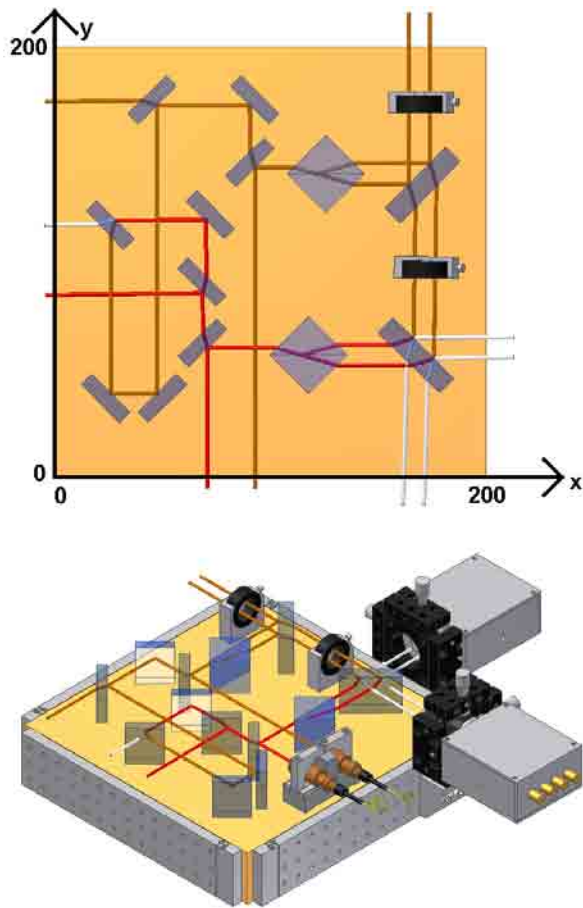


Figure 1: Top: view from above on the interferometer board; bottom: assembly of the interferometer with frame and quadrant photo-detectors.

The positions of the optical components are determined by working on two planes. It was possible to plan the position of the substrates on a single plane and to draw the optical path of the laserbeams on another plane, 20 mm (beamheight) above the first one. The interferometer layout is adapted from the aluminum interferometer setup, including single-element photo-detectors for intensity stabilization and frequency phaselock and two quadrant photo-detectors for the translation and tilt measurement. In this design, care is taken, that the optical path of the beams from fibers to their su-

perposition on the quadrant photodetectors is equal to the optical path from fibers to their superposition on the phaselock beat diode. All substrates are wedged by an angle of 1° preventing reflections on the backsides of the substrates which could lead to perturbations on incoming beams. For exact positioning of the optical components on the Zerodur baseplate, a CCD based read-out was developed.

Figure 1 (bottom) shows the full assembly of the new interferometer with bonded frame and mounted angles for lens holders. With these lens holders the RF quadrant photodetectors can be adjusted relative to the laser beams on the board.

Integration

To integrate the optical components on the Zerodur board a special adjustment tool was developed. The optical elements are placed in a holder which can be moved very precisely by adjusting screws (translation in x, y and z; rotation). The optical component is hold by small magnets. A CAD drawing of the tool is shown in figure 2.

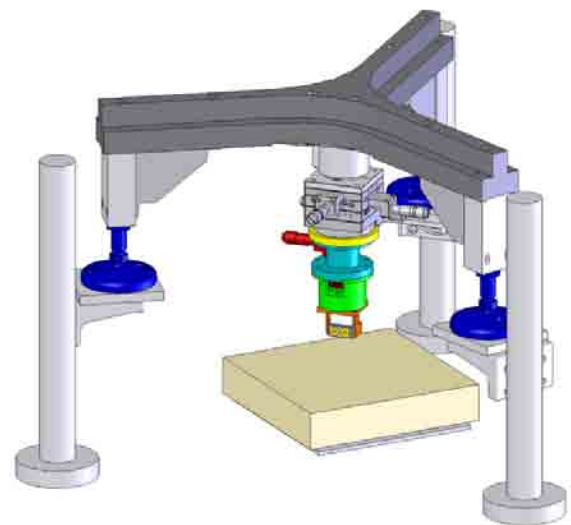
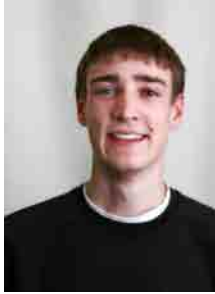


Figure 2: CAD model of the adjustment tool.

Development of RF Quadrant Photodetectors

Steffen Wälde, Martin Maurer, Hans-Reiner Schulte, Ulrich Johann, Claus Braxmaier, and Dennis Weise



We built a quadrant photodetector for LISA with a very flat frequency response and a constant phase shift at 1064 nm. This detector has a DC-path for frequencies from DC to 20 kHz and an AC-path for frequencies between 2 and 20 MHz. The sensitivity of the AC-path is between 814 nW and 1.3 μW, the sensitivity of the DC-path is between 13.5 μW and 1.6 mW. A quadrant photodiode is used for the technique of differential wavefront sensing. The two paths are for each of the four quadrants present. For differential wavefront sensing the phase of all quadrants has to be identical so the electronic design and the PCB layout of every channel has to be as equal as possible.

Introduction

The LISA mission as a space-based gravitational wave detector aims to detect gravitational waves in a frequency band from 0.1 mHz to 1 Hz. Three satellites arranged in a nearly equilateral triangle with an edge length of about 5 million km will fly in an earth-trailing orbit around the sun. The distance between the satellites will be measured with an interferometer setup. During the mission the distance between the satellites varies with about 50000 km which causes a Doppler shift of the laser frequency in a range of 2 to 19 MHz.

In this context we developed a RF low noise quadrant photo detector which is suited for high precision phase measurements in a sub-Hz LISA measurement band. It uses an Indium Gallium Arsenide quadrant photodiode with a total diameter of 1 mm. The detector as a position sensitive device can also be used for the technique of differential wavefront sensing. With respect to the mission requirements the detector has a constant frequency response and a linear phase response for frequencies between 2 and 20 MHz. It has also a path for frequencies between DC and 20 kHz for each quadrant. The following sections show the electrical setup and the current measurements.

Detector Design

In the interferometer setup the two laser beams have different frequencies ω_1 and ω_2 . The beams can be described with the equations 1 and 2. The superposition of the beams arises from equation 3. For this reason we developed two circuits which can detect AC and DC signals.

$$\mathbf{E}_1 = E_1 \cdot e^{j(k_1 z_1 - \omega_1 t + \varphi_1)} \quad (1)$$

$$\mathbf{E}_2 = E_2 \cdot e^{j(k_2 z_2 - \omega_2 t + \varphi_2)} \quad (2)$$

$$|\mathbf{E}_{\text{ges}}|^2 = |\mathbf{E}_1 + \mathbf{E}_2|^2 = \underbrace{E_1^2 + E_2^2}_{\text{DC signal}} + \underbrace{2E_1 E_2 \cos[(k_1 z_1 - k_2 z_2) - \Delta\omega t + \Delta\varphi]}_{\text{AC signal}} \quad (3)$$

The AC-path which is the main measuring channel filters the AC signal in a range of 2 to 20 MHz. The filter of this path consists of the capacitance of the photodiode, an inductance and a second capacitance. The main task of the filter is forming the frequency response. The signal level is adapted to the AD converters of our FPGA board.

The DC-path detects the DC signal and frequencies up to 20 kHz of the AC signal of equation 3. We can use this path with our old interferometer setup which has a beat frequency $\Delta\omega$ of 10 kHz

and to monitor optical intensity.

For optimal performance at 1064 nm indium gallium arsenide (InGaAs) quadrant photodiodes are used. InGaAs Diodes have a responsivity of $0.7 \frac{A}{W}$ at 1064 nm. The used quadrant diodes have an optical sensitive area with an active diameter of one millimeter since the laser beam of our interferometer setup has a diameter of 1.5 mm. For a stable bias generation a high precision 5 V voltage reference (AD586) is used.

For best RF shielding a 4-layer PCB-layout is used. The AC-path on the top layer is shielded from the other layers with a ground-plane between the top layer and the other layers. The third layer is used for the power supply and the connection of the PT100 temperature sensor. Ground connections are realized with vias to the ground-plane so that the way to ground is as short as possible. The fourth layer (bottom layer) is used for the DC-path and the bias generation. Figure 1 shows a quadrant photodetector mounted on a part of its housing. In our layout only SMD (Surface Mounted Device) parts are used.

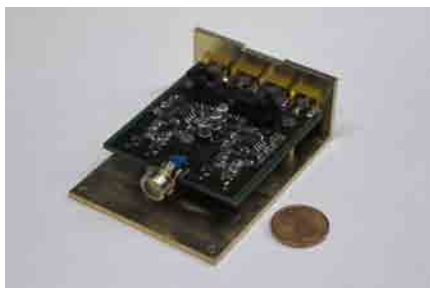


Figure 1: Photo of a quadrant photodetector

Results

In this chapter we present the test of the detector. First we measured the electronic performance without the photodiode. With a BNC connector and a 20 pF capacitor soldered on the PCB we simulated the photodiode. Over the BNC connector a test signal for the electronic measurements was introduced. After the electronic measurements the photodiode was soldered in for optical measurements. For testing the electronic assembly, we used a network analyzer to measure the phase and the frequency response of every quadrant. For AC measurements a HP8753A network analyzer is used.

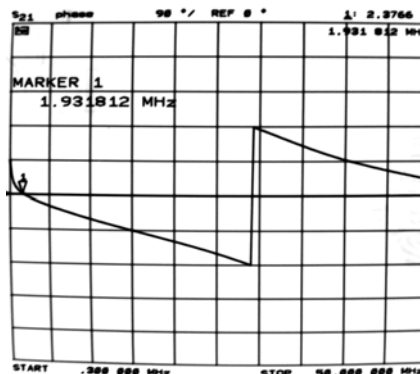


Figure 2: The measured linearity of the AC-path

The phase response of one AC-path is shown in Figure 2. The plot shows the phase shift from DC to 50 MHz. In a range of 2 to 20 MHz the phase response is linear.

The noise measurements of the DC-path were made with our phasemeter. With the phasemeter we sampled with 20 Hz while a laser beam with a beat-frequency of 10 kHz was pointing on the photodiode. While this measurement the whole beat setup and the detector were in a vacuum chamber at $4.6 \cdot 10^{-3}$ mBar. A plot of the result is shown in Figure 3.

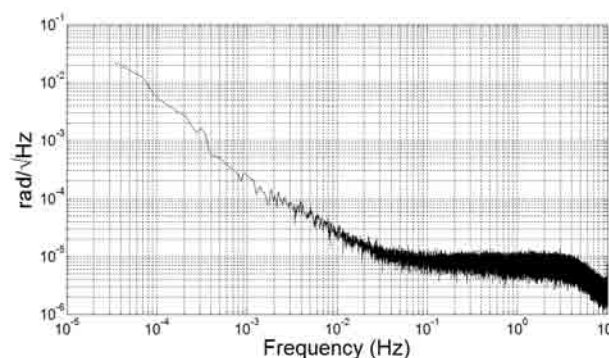


Figure 3: Noise measurement of the DC-path. In the Figure the PSD of the phase difference of quadrant A and quadrant B is shown.

Outlook

Up to now we produced four quadrant photodetectors. For the next time we plan noise measurements of the AC-path with the new phasemeter and the same setup, but with a 10 MHz beat signal instead of 10 kHz. Furthermore we want to measure the crosstalk between the AC und DC channels and the signal-to-noise ratio (SNR).

Development of an Ultraprecise Digital RF Phasemeter

Markus Wussler, Franziska Kittelmann, Martin Gohlke, Hans-Reiner Schulte, Ulrich Johann, Claus Braxmaier, and Dennis Weise



The future LISA Mission requires an ultraprecise phasemeter for acquisition of interferometer beat signals with μrad precision whose differential phase contains information about the distance fluctuations between two satellites. This article presents the concept of the new phasemeter. First we show the principal idea and the first design of the PLL (Phase Lock Loop). Finally, we present the current status, show some performance measurements and give an outlook of the next planned steps.

Introduction

LISA is an ESA/NASA mission with the scientific goal, to measure gravitational waves in a very low frequency band from $30\ \mu\text{Hz}$ to $1\ \text{Hz}$. Therefore it is necessary to measure a variation of the distance between two satellites in the range of picometers. There are three satellites grouped in an equilateral triangle with a relative arm length of 5 million km. The constellation follows the earth in a distance about 50 million km. To reach the picometer accuracy, a heterodyn interferometer setup is used. The output of the interferometer is a sinusoidal signal. The phase of this signal contains the information about the displacement of the satellite. A phasemeter was developed over the last years and is currently under investigation. With our prototyp of a phasemeter, based on a FPGA (Field Programmable Gate Array) the phase of two signals can be measured and thus the changes of distance can be calculated.

Requirements

The phasemeter's goal is to determine the phase of signals in a frequency band from 2 to 20 MHz with μrad accuracy. To realize this a high precision phase locked loop phasemeter implemented in a FPGA

is needed (see Figure 1). In the current setup a Stratix II Developmentboard is used as FPGA. It has two AD Converter inputs with a sampling rate of 100 MHz. Every 100 ms the phase and frequency will be read out via RS232. This lead to a data reduction up to 10^7 . On the computer a self written C-program will save the incoming data stream for post processing analysis.

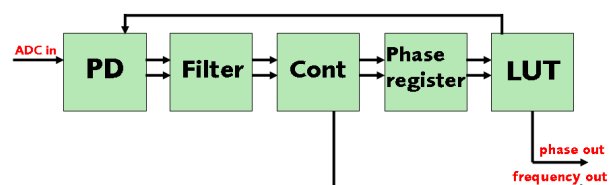


Figure 1: Logical design of the PLL. PD phase detector, Cont controller, LUT look up table

Layout and Function

The main items of the phasemeter are two parallel working PLLs. For future studies the number of PLLs will be extended. The analog signal will be digitalized by 12 bit ADCs with a sample rate of 100 MHz. The digitalized signal is the input for the first stage of the PLL, the phasemeter (PD). It

multiplies the incoming signal (f_1) with a signal (f_2) from a NCO (Numerical Controlled Oscillator). The resulting sinusoidal signal contains the sum ($f_1 + f_2$) and the difference ($f_1 - f_2$) of both signals. The following low pass filter is separating the DC (diff) and the AC-Part (sum). The DC-Part is used as the input signal for the controller and contains information about the difference of the phase. The controller is connected to a phase register. The phase register works like a counter and is referencing the controller to the Look-Up-Table (LUT). The LUT, the controller and the phaseregister constitute the numerical controlled oscillator. The error signal and the NCO frequency signal from the controller output contains the phase and frequency information of the input signal from our measurement signal. Both information will be decimated by a filter and send to the RS232 Interface.

Implementation

The phasemeter firmware is written in VHDL (Very High Speed Integrated Circuit Hardware Description Language). It is separated into logical function blocks stored in a self generated library. Thus it is possible to duplicate and combine the single blocks very easily. Every block just have to be instanced in the main program and the compiler will generate the signal path in the register transfer level. All variables and components are defined in a global variable level. The development of this enviromental structures was one of the main challenge of the last year activities, but now it makes it comfortable to accomplish any kind of changes. The datablock accumulates the measurement signals from the different PLLs and send them to the RS232 interface. The computer uses a self developed C-program to store the data stream in a text file which will be used for post processing analysis.

Current Performance

After a successful implementation of the PLL in the FPGA we have started performance measurements. The most important characteristic is the difference

between the phases of the PLLs. To reach the LISA measurement requirements it is necessary to measure with the accuracy of $6 \mu\text{rad}$ within the LISA band from 0.1 mHz to 1 Hz. (see Figure 2) We already reach this level for the most parts. For the measurement we connected the input of both PLLs with the same frequency generator to get the same signal on both ADCs. As a conclusion we can say now, that currently the limiting factor is the jitter of the ADC's.

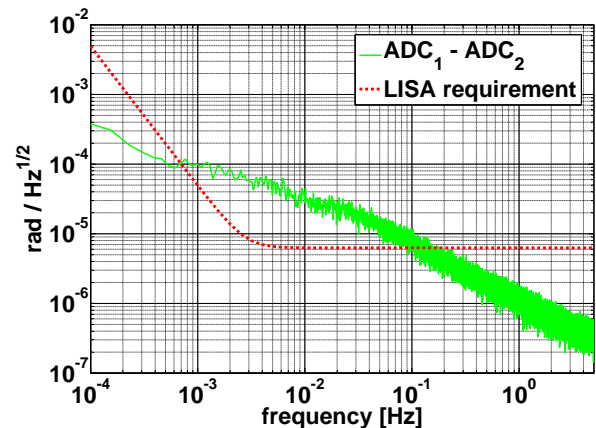


Figure 2: The graph shows the $\text{PSD}^{\frac{1}{2}}$ of phase difference between the two input signals

Outlook

At the moment two signals can be measured with an accuracy close to fulfil the LISA requirement. As the next step we will extend our system to get more channels (8, 16 or 32 input signals). For this reason we need a new development platform to get more extension options to connect ADCs. If eighth ADCs and PLLs will be implemented, it is possible to use the phasemeter the first time with our RF quadrant photo detectors. To fulfil the requirements totally, it is necessary to work on the ADCs. Thus we would implement better ADCs with less jitter effects. Another approach is to mix the analog input signal with a pilot tone, that will give us information about the phase offset affected by the ADCs. In real time there will be made an internal correction with a second PLL.

Laser Frequency Stabilization to Optical Resonators

Felix Rey, Martin Gohlke, Hans-Reiner Schulte, Ulrich Johann, Dennis Weise, and Claus Braxmaier



High-precision interferometry – as it is used for the LISA-Mission – requires highly stable laser frequencies. Common lasers emit light over a short spectral range (small line width) and for most applications the light can be approached as monochromatic. But in order to cope with the high requirements of the LISA-Mission, the laser line width – and also laser frequency drifts over long time scales – have to be further reduced. Therefore, the laser frequency has to be stabilized using a feedback control system. As reference either an atomic or molecular transition or an optical resonator can be used. The Laboratory of Enabling Technologies already possesses a system locked to a transition of iodine, to achieve long-term stability. But on short time scales, frequency stabilizations to optical high-finesse resonators provide best results. Therefore two laser stabilization setups based on optical resonator are going to be realized. In the following, the initial work for these setups is outlined.

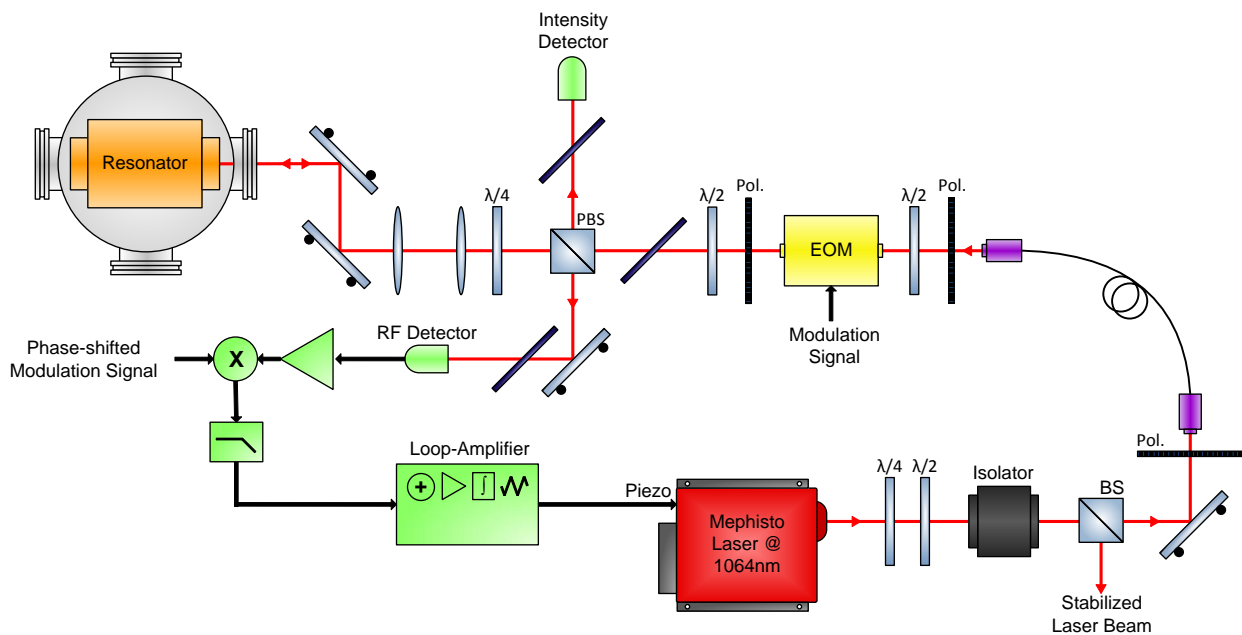


Figure 1: Pound-Drever-Hall setup for laser frequency stabilization using an optical high-finesse resonator (EOM - electro optic modulator, BS - beamsplitter, PBS - polarized beamsplitter, RF - radio frequency, Pol. - polarizer)

In our setup we use the most common technique for laser frequency stabilization based on optical resonators, the Pound-Drever-Hall method. A schematic of our whole setup is shown in figure 1. The isolator protects the laser from back reflexions and the beam splitter (BS) reflects part of the light for further purposes. In order to achieve flexibility,

the stabilization setup is connected via an optical fiber.

After fiber output, the phase of the light is modulated by an electro-optic-modulator (EOM). The polarizing beamsplitter (PBS) separates a part of the incoming beam to measure the intensity on the photodetector. Later this signal can be used for an

additionally intensity stabilization. The transmitted part of the light is sent to the resonator. In order to minimize environmental influences, the resonator is protected in a high vacuum chamber. The pair of two lenses matches the Gaussian beam to the eigenmode of the resonator. After passing twice the $\lambda/4$ -waveplate, the polarization of the beam reflected by the resonator is rotated by 90° and is deflected to the RF single-element photodetector, which is an offshoot of the RF quadrant photodetector. The tilted components in front of the detectors and the PBS are ND-filters, which attenuate reflexions. The electric signal of the RF signal for frequency stabilization is amplified and mixed with a sine signal at the EOM modulation frequency whose phase relative to the EOM driving signal can be adjusted. After low-pass filtering, the resulting signal is used as error signal for a feedback control systems. In figure 2 its mathematical prediction is illustrated. With altering phase-shift between the modulation signals of the mixer and the EOM, the slope around the operation point varies. For best sensitivity, the slope should be maximal.

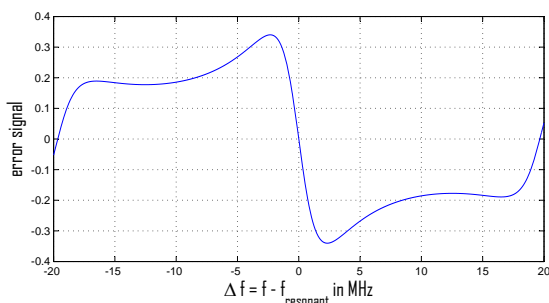


Figure 2: Calculated error signal using Pound-Drever-Hall technique.

The error signal is input to a P-I control electronics which actuates the laser frequency via a piezo which performs pressure on the laser-crystal and alters the emitting frequency. A disadvantage of the fast piezo actuation is the small range of frequency variation. Therefore the setup can be extended with another Loop-Amplifier, which takes the piezo-signal and regulates the temperature of the laser crystal. This slow actuation copes with large frequency drifts.

Resonator Mounting

The mounting of the resonator has to protect the resonators from soiling, minimizes vibrations and guarantees a benign temperature environment. Moreover it has to mount the resonator without deforming it. In figure 3 an explosion drawing of the mounting is shown.

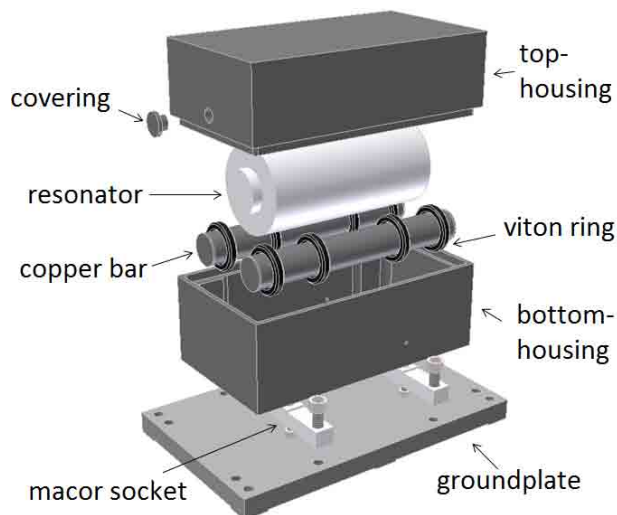


Figure 3: Explosion drawing of the setup for resonator mounting.

Between the aluminum groundplate and the bottom-housing, macor sockets function as thermal washer. Macor is a glass ceramic with ultra low thermal conductance. The bottom- and top-housing and the bars under the resonator are made out of copper in order to guarantee a uniform temperature around the resonator. The resonator lies on the middle two viton rings, which are pinned on the copper bars. Viton is a vacuum suitable fluoroelastomer. The exterior rings are supported by the bottom-housing. The bars are hollow and filled with silica sand. Together with the double viton supporting, this minimizes vibrations of the resonator. The top-housing has two holes, one for the transmitting and one for the reflected beam.

The whole resonator mounting is built in a vacuum chamber and wrapped in MLI-foil to get additional protection against external influences. In the last months of 2009 nearly all components for both frequency stabilization setups were procured. In the first quarter of 2010, a working setup of one laser frequency stabilization is intended.

Validation of In-Field Pointing Concepts for LISA

Andreas Keller, Daniel Küsters, Martin Gohlke, Ulrich Johann, Claus Braxmaier, and Dennis Weise



For 'In-Field Pointing' mechanism (IFPM) – an alternative solution for steering the line of sight on LISA mission – a piezo linear motor is characterised. It is designated to actuate a small mirror located in the pupil plane of the telescope which defines some requirements on travel range and position accuracy. Measurements of pin motion are performed with the internal linear encoder and a sub-nanometer heterodyn interferometer. After an introduction to the topic the actuator is presented. In the following the test setup, first results and a summary is given.

Introduction

'In-Field Pointing' is an alternative payload concept for LISA mission which is used for steering the lines of sight of the two telescopes to compensate for constellation breathing. This done directly by a small, actuated mirror located in an intermediate pupil plane of the telescope [1].

A possible candidate for actuator is a Nexline N-111 of PI which may deliver the requirements for travel range and position accuracy. This device is characterised in cooperation with TNO in Delft on the aspect of operation for this purpose.

In the next sections the actuator is described, followed by a short description of the measurement setup and first results.

Nexline actuator

The Nexline actuator is a piezo linear motor which moves a pin with several stacks of piezos [2]. A piezo stack consists of a shear piezo, which is used to shift the pin, and a clamp piezo which controls the mechanical contact of shear piezo with the pin. The pin can be moved in two different modes. In the precise positioning mode only the shear piezos are actuated. When commanded position exceed the travel range of the shear piezos the piezos have to

hand-over which is also called step mode.

The actuator is commanded with a controller responsible for voltage management and closed loop operation (when equipped with a linear encoder for position response). Both devices are shown in figure 1. The actuator has a resolution of 5 nm in closed loop operation.



Figure 1: Nexline actuator and controller

Setup

The movement of the actuator are characterised by two different ways, the internal linear encoder and a high precision heterodyne interferometer with a noise floor in the subnanometer range. With the interferometer the angle of the mirrors can also be measured.

The typically used measurement procedure is as follows: The velocity and end position is commanded to the controller which autonomous approaches the position (in closed-loop operation). It chooses automatically the mode and makes steps if necessary.

During the movement the actual position measured by linear encoder or interferometer is constantly recorded.

Results

The following section presents first results obtained by both linear encoder and interferometer.

Hand-over of piezos

Every 3.3 μm the shear piezos have to perform a step which leads to short displacement of the pin in the order of 1 – 2 μm (see figure 2). These displacements are independent on velocity and go back to original position due to the closed loop operation.

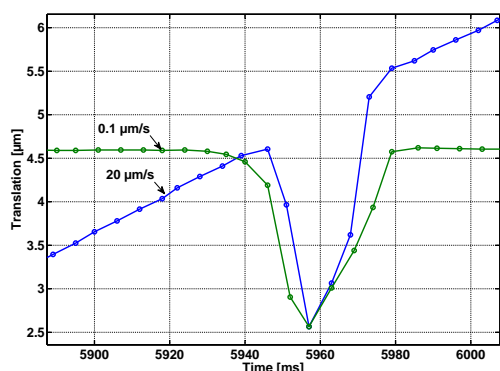


Figure 2: Hand-over process with two different commanded velocities (0.1 $\mu\text{m/s}$ green and 20 $\mu\text{m/s}$ blue curve).

Vibrations on setup

The interferometer is able to measure tilt of a fixed mirror mounted on the Nexline support. Two peaks are visible in figure 3 which coincide with start and end of hand-over process. This is presumably due to lift and reclamp of piezo stacks releasing tensions on the pin which causes vibrations on the entire mount.

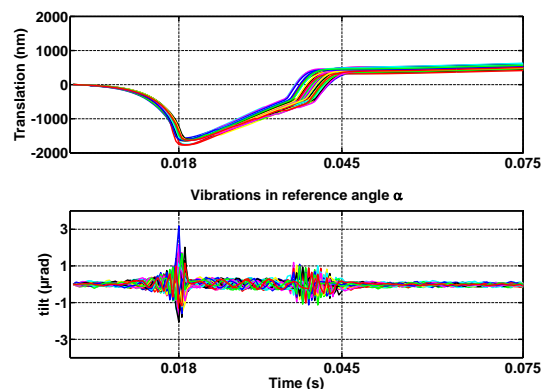


Figure 3: About 30 step events shown. Upper part: translation of pin mirror, lower part: vibrations in angle of fixed reference mirror. The vibrations coincide with start and end of step process.

Nonlinearities on trajectory

The controller is optimised to obtain a constant velocity of pin movement. But it turned out that the velocity can be different than the commanded. This happens on a short period of time midway of two steps. The origin of this nonlinearity is unknown.

Summary

During the tests, several serious performance limitations are determined. With regard to In-Field Pointing there exist two possibilities, searching for another actuator complying better with requirements or elaborate a workaround for the limitations.

The next steps will be to investigate for an alternative actuator and to characterize other parts of the IFPM, for example the mirror surfaces. In the process it is planned to move the mirror laterally relative to the interferometer and measure the surfaces unevenness in the picometer range.

Bibliography

- [1] Astrium GmbH and TNO Delft. *Antrag auf Zuwendung: Validation of In-Field Pointing Concepts for LISA*, 2008.
- [2] PI. *PZ161E User Manual, E - 755 Digital Controller for Nexline Linear Drives*.

Investigations towards μN High Efficiency Multistage Plasma Thrusters

Andreas Keller, Marcel Berger, Davar Feili, Dennis Weise, Ulrich Johann, and Claus Braxmaier



Future space missions in earth observation and science are based on high accuracy metrology payloads, mostly in combination with drag free attitude control of the spacecraft. Goal is to ensure an appropriate noise-free environment for the sensitive measurements of for example Earth's gravity field and its gradient, gravitational waves or Earth's magnet field. For that purpose thrusters with μN thrust and minimum noise are required. Different kinds of thrusters are currently on development (RITs, FEEPs, GITs) with great difficulties in lifetime and noise behavior. In this report we present the initial work with respect to a feasibility study of HEMP (**H**igh **E**fficiency **M**ultistage **P**lasma) thrusters down-scaled to the μN -region. An introduction to the principle is given and first test results of a prototype are presented.

Introduction

In the last decades electric propulsion was used in many satellite missions flying in space. The first ideas lies 100 years behind.

The major advantage of electric propulsion in comparison to chemical thrusters is the high efficiency in using propellant. Another point is the lower disturbance of the spacecraft's instruments due to lower thrust noise and mechanical vibrations. Their main field of application is attitude and orbit control (such as north-south station keeping) and as main engine on interplanetary spacecraft.

Upcoming ideas and plans for constellation missions increased the need for precision positioning and so the necessity for low noise as well as low thrust propulsion. However there exist until today no long-life low thrust device with high efficiency. So there is the idea to investigate the HEMP thrusters [1] for their scalability to the low thrust area.

HEMP Thruster

There are many different classes of ion thrusters known. One of the most promising is the HEMP thruster. The schematic setup is shown in Figure 1.

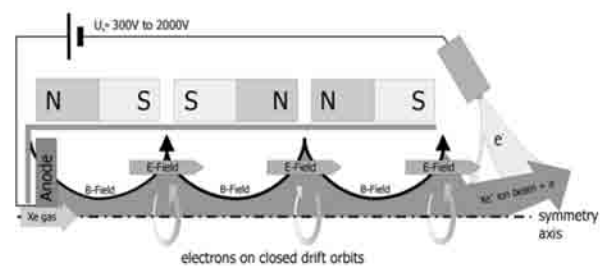


Figure 1: HEMP thruster operation principle [2].

In a cylindrical dielectric tube a gas (typically a noble gas, in the figure Xenon) is injected. Electrons generated by a neutraliser and attracted by the anode (placed at the gas inlet) ionize the gas by impact (generation of ions). These ions are accelerated in the electric field (several hundred V up to a few kV).

A periodic poled magnet (PPM) stack is used to focus the plasma beam which reduces erosion of the walls. It also traps electrons on their way to the anode in magnetic cusps which increases ionization efficiency of the electrons. Between two magnets the magnetic field has a predominantly radial character. Due to Lorentz force ($\mathbf{F} = q(\mathbf{E} + \mathbf{v} \times \mathbf{B})$) the electrons are on a spiral movement and increase the collision length. The increased electron density shields the electric field so that after every stage the acceleration voltage drops.

The neutraliser emits electrons and is employed

for discharge ignition and beam neutralisation (to prevent charging of spacecraft). The advantages over other thrusters like GIT's (**Grid Ion Thruster**) and FEEP's (**F**ield **E**mission **E**lectric **P**ropulsion) are:

- simple design
- high reliability
- high efficiency (conversion of 80 % of electric power in kinetic ion beam power [3])
- low sputter erosion of the tube walls or grids

Therefore this class is an interesting design for further investigations, as the above features are extremely relevant for space applications.

The Project

We designed and manufactured a breadboard model to study the properties of these thrusters in the low thrust area. A CAD drawing cross section is shown in figure 2. The main focus is laid on flexibility so that different geometries can be easily tested. The static magnetic field created by permanent magnets is simulated to optimise cusp fields.

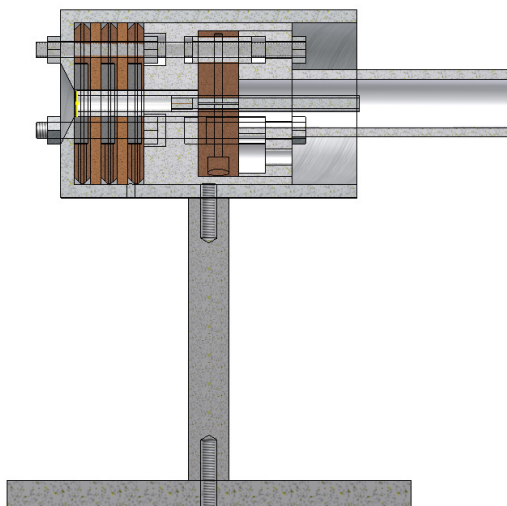


Figure 2: CAD drawing cross section of HEMP thruster.

First tests are already passed. The range of stable operation is around anode voltage 650 V, chamber pressure 5×10^{-3} hPa and Xenon mass flow 0.8 – 1.5 sccm. The operating thruster with a light bulb as neutraliser is shown in figure 3.



Figure 3: HEMP thruster in operation. Neutraliser is a light bulb.

The next steps are varying parameters and checking thruster performance as well as improving the test facility (lower base pressure with a more powerful vacuum pump). The goal is to design an advanced thruster.

Bibliography

- [1] G. Kornfeld, N. Koch, and G. Coustou. The highly efficient multistage plasma (HEMP) thruster, a new electric propulsion concept derived from tube technology. 4th IEEE International Conference on Vacuum Electronics, 2003.
- [2] N. Koch, H.-P. Harmann, and G. Kornfeld. Development and test status of the thales high efficiency multistage plasma (HEMP) thruster family. 29th International Electric Propulsion Conference, 2005. IEPC-2005-297.
- [3] J. A. Eichmeier and M. Thumm, editors. *Vacuum Electronics*. Springer Berlin Heidelberg, 2008.

High Precision Optical Metrology

Thilo Schuldt, Klaus Ergenzinger, Ulrich Johann, and Claus Braxmaier



The ESA project 'High Precision Optical Metrology (HPOM-2)' is a breadboard-level technology demonstrator for future formation-flying missions where distances between two spacecraft with separations up to a few hundreds of meters have to be measured with high accuracy. Examples of relevant space missions are the aperture-synthesis space-telescope Darwin and the sun coronagraph mission PROBA-3. In these applications, the requirements in distance metrology can only be met using optical methods, i. e. laser interferometry. HPOM-2 represents a dual wavelength interferometer (DWI) with a distance resolution better $10 \mu\text{m}/\sqrt{\text{Hz}}$ and an operational measurement range of 0 m to 250 m. Astrium GmbH – Satellites is in charge of the development of the DWI laser assembly based on the results of the HPOM-1 program. An optical setup using two phase-locked Nd:YAG NPRO-type lasers was set up, where the frequency generation part utilizes fiber-optic components such as AOMs, polarizers and detectors. A static distance measurement over 25 h was carried out using a fiber-optic optical head dummy, showing a $12 \mu\text{m}$ rms noise level well within the specifications.

An artist view of the planned formation flying mission PROBA-3 is shown in figure 1. Two spacecraft, flown in a distance of approximately 150 m, form a coronagraph where one spacecraft carries the occulter casting a shadow over the second spacecraft carrying an optical bench with associated electronics and detection hardware. The distance measurement



Figure 1: Artists view of the PROBA-3 mission. Two spacecraft in a distance of ~ 150 m form a coronagraph where one spacecraft carries the occulter and the other the optical bench, electronics and detectors (figure: ESA).

between the spacecraft is carried out using a dual-wavelength interferometer with a required distance resolution below $10 \mu\text{m}/\sqrt{\text{Hz}}$, an operational measurement range of 0 m to 250 m, an unambiguous longitudinal measurement range of ± 25 mm and a longitudinal drift measurement capability up to 250 mm/s.

Experimental Setup

The DWI setup uses two phase-locked Nd:YAG lasers at a wavelength of 1064 nm. One of the lasers can optionally be frequency stabilized to a hyper-fine transition in molecular iodine using modulation transfer spectroscopy at 532 nm (second harmonic). The frequency offset between the two lasers is set to 3 GHz which corresponds to a synthetic wavelength of 10 cm. The light of both lasers is fiber-coupled and a fiber-optic setup utilizing 3 acousto-optic modulators (AOMs, used as frequency shifters and operated at frequencies of 75 MHz, 76.9 MHz and 79 MHz) yields to two independent (relative) interferometric measurements. Two InGaAs photodetectors detect the heterodyne signals at 1.9 MHz and 4 MHz, respectively, which are input to a dual heterodyne phasemeter developed by SIOS Messtechnik (Ilmenau). The phase measurement is based on

two internally synchronized digital PLLs. The obtained distance data is read out using a standard PC by RS232 interface. A photograph of the laser setup including phase-lock detector and of the fiber-optic setup for frequency generation is shown in figure 2.

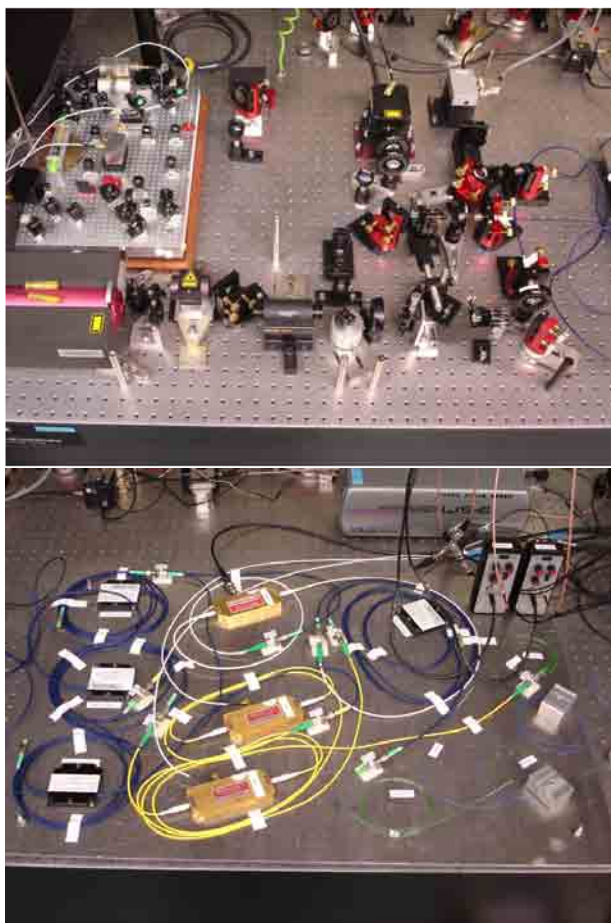


Figure 2: Photograph of the lasers (top) and the fiber-optic setup for frequency generation (bottom).

Measurement Results

A long-term measurement with a pigtailed free beam combiner as dummy optical head is shown in figure 3. Fiber polarizers are used in front of the

dummy optical head, the optical power at each detector is approximately $800 \mu\text{W}$. Although the measurements were carried out under harsh conditions (several K difference in room temperature), no clear thermal sensitivity can be observed. The RMS value in distance is $12 \mu\text{m}$ over the full 25 h measurement time – and therefore compliant with the $32 \mu\text{m}$ specification. In our measurements, it was seen that the implementation of (fiber-)polarizers at the output of the frequency generation part is essential for minimizing the temperature sensitivity.

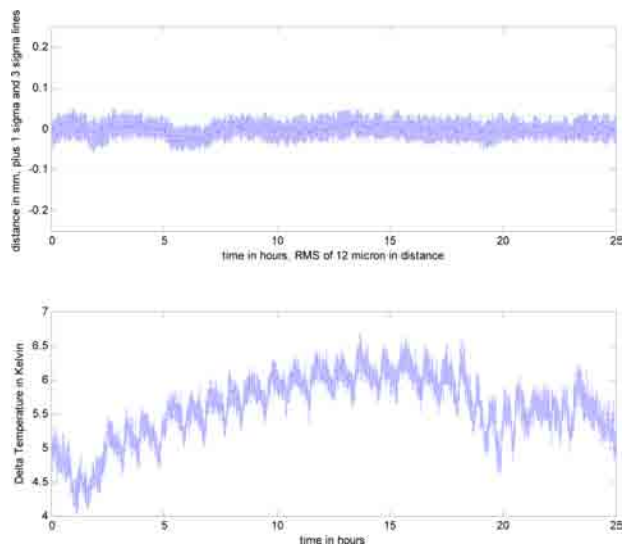


Figure 3: Long term static distance measurement of the DWI. The upper curve shows the measured distance (with included 1σ and 3σ lines), the lower curve the room temperature.

This project is carried out under ESA contract 20864/07/NL/SFe. The DWI laser assembly is developed by Astrium GmbH – Satellites (Friedrichshafen) with SIOS Messtechnik GmbH (Ilmenau) responsible for the phasemeter update. The laser assembly will be integrated with an optical head developed by Astrium SAS (France) and tested at TNO (Netherlands).

Measurements on Single Mode Waveguides in a Mid-Infrared Test Interferometer

Reinhold Flatscher, Stefan Ziegler, Dennis Weise, Ulrich Johann, and Claus Braxmaier



One of the key elements of the Darwin instrument is a single mode wavefront filter used to cancel star light and to detect the weak light from Earth-like planets. We manufactured short single mode fibres acting as perfect wavefront filters. Extruded silver halide fibres can be used over the full wavelength band of Darwin. In the lower subband optional fibres drawn from special glass (GAST) can be employed as well. The performance of the produced devices was characterised in a representative mid infrared interferometer. The fibres were exposed to gamma radiation without degradation and survived a cryogenic test at 10 K. Silver halide fibres with multilayer AR-coating and special cladding mode absorption layers were manufactured with high yield. They offer low insertion loss together with single mode light transportation.

Introduction

The objective of the Darwin Mission is to search for signs of extra-terrestrial life on foreign planets. Darwin is a space program of the European Space Agency - ESA. NASA plans a similar mission called TPF (Terrestrial Planet Finder). The final mission, most likely a collaboration of ESA and NASA, shall detect and in a second step chemically analyse the atmosphere of Earth-like targets. One of the main mission goals is to identify bio markers like water vapour, ozone, and carbon dioxide as shown in Figure 1 sketching the typical emission spectrum of our Earth.

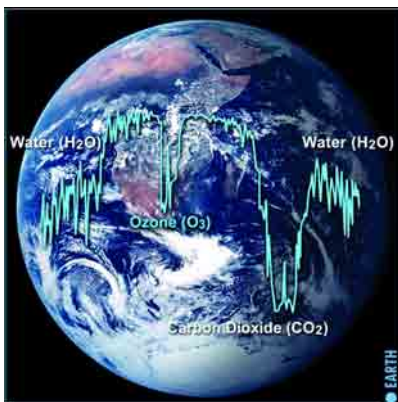


Figure 1: Spectral signature of our Earth. Courtesy of ESA.

Looking on a star/planet system the star light must be reasonably suppressed to make visible the weak radiation from a "warm" planet orbiting around the star within the habitable zone. High quality nulling interferometers are used to suppress the star light by destructive interference.

Setup

The Darwin Mission relies on a nulling interferometer coupling together 4 free-flying telescopes. Operating in the mid infrared the nulling requirements can be relaxed to 10^6 . Using wavefront filters allows to employ optical elements of standard precision.

The performance of the realised wavefront or mode filters is measured by using a compact and fully representative Mach-Zehnder interferometer as shown in Figure 2. A short piece of single mode fibre is the optimum wide band wave front filter as it suppresses low and high order wave front errors in contrast to pinholes that reduce high frequency errors alone.

The light is coupled into the thin core of a single mode fibre. The core is surrounded by cladding with lower refraction index and this step-index structure ensures the guided propagation of light through the core. Light of longer wavelengths extends much into the cladding and higher-order cladding modes

may be generated due to limited cladding extent and/or short fibre length. Cladding modes are suppressed by additional damping layers attached on the cladding. Different fibre materials are used in the interesting wavelength range. Special glasses made of germanium, arsenic, selenium, and tellurium (GAST) are preferred in the lower band between 6.5 μ m and 11 μ m as they can be drawn like silica fibres. In the upper band between 10 and 20 micron extruded polycrystalline silver halides are the best choice. Silver halide is also a promising candidate for the lower Darwin band.

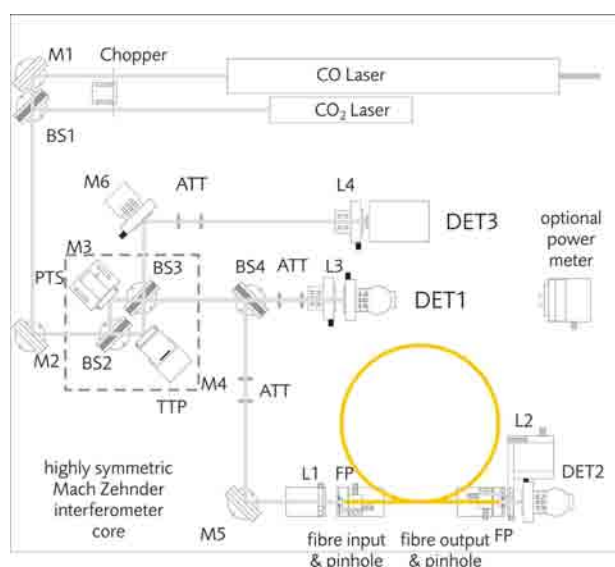


Figure 2: Highly symmetric Mach Zehnder interferometer used for testing the mode suppression capability of the realised waveguides. Mx redirection mirror, ATT attenuator of reflective type, PTS piezo translation stage (OPD), Lx lens, TTP tip/tilt piezo stage, DET detector, BSx wedged beam splitter

Performance and Environmental Tests

The following fibre performance parameter can be routinely verified:

- mode distribution by matrix camera at two different wavelengths
- attenuation of the fibre at the two different wavelengths
- suppression of star light at both wavelengths by using the interferometer

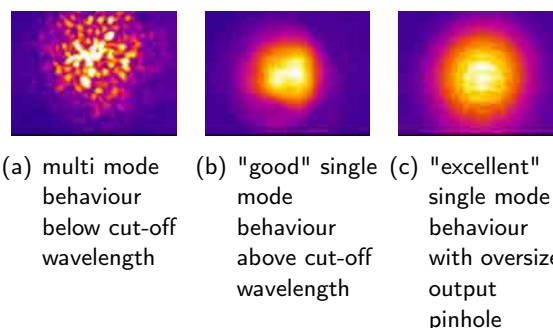
- prove of single mode capability

The following environmental tests were performed:

- cryogenic temperature test at 40 K (typically less than 10 K)
- vacuum test to verify the reliability of the used materials and coatings
- γ -radiation test with total dose of 50 krad (done at ESA's cobalt 60 facility)
- high-energy proton radiation test (done at PSI)

Results

Figure 3 illustrates typical results seen by the matrix camera indicating a clear multimode (left), a starting single-mode situation (mid), and the desired clean single mode (right). The fundamental mode of a single mode fibres manifests as a Gaussian-like intensity distribution of the emitted beam. Non-perfect mode cleaning of very short fibres can be still improved by an oversized pinhole at the fibre's output.



(a) multi mode behaviour below cut-off wavelength
 (b) "good" single mode behaviour above cut-off wavelength
 (c) "excellent" single mode behaviour with oversized output pinhole

Figure 3: Typical mode distributions recorded at fibre output.

Fresnel losses at both fibre facets of 12.5% in Ag-BrCl and 17% in GAST glass are further reduced to a few percent by applying multilayer AR-coatings.

Figure 4 shows a photograph of a typical fibre cable batch. All fibres are AR-coated, they do have cladding mode absorption layers, the fibre ends are polished and are fixed in ceramic or metal ferrules as part of SMA connectors. The thin fibres are protected by plastic tubes to avoid bending or breaking during handling.

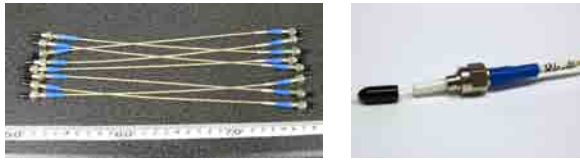


Figure 4: Fully assembled polycrystalline fibre samples and details of fibre end.

A dip stick has been manufactured to perform the cryogenic temperature test. The stick with the fibre sample in its inner part is plunged in a storage vessel filled with liquid helium. Controlled flooding of the vacuum inside the stick with helium adjusts the sample temperature. Figure 5 shows the fully dipped stick in thermal equilibrium.



Figure 5: Dip stick with fibre sample on 10 K level during live test.

Conclusion

In the 3 years activity we could improve the performance and quality of the manufactured fibres and the production yield. Circular cores and good optical contact between core and cladding are routinely achieved now.

The fibre made of soft silver halide achieved good results. Silver halide fibres are extruded by pressing the heated soft material through a die under high pressure. High facet quality and optimised material parameters finally yielded single mode behaviour together with low damping. The material is well suited for the entire Darwin wavelength band. The core/cladding dimension is 50/500 micron. We measured mode suppressions of 15,000 and intrinsic fibre transmissions in the order of 0.7 to 4 dB/m. The typical length of a single mode waveguide is 25 cm. 17 sample cables passed the performance tests and are compliant to the requirements.

GAST fibres are more difficult in manufacturing as the glass is brittle and non-laminar flow during the drawing prevents core forming. Excessive purification is required to obtain flat spectral transmission here.

Outlook

Silver halide fibres are the best choice for Darwin's wavefront filters. Many fibres passed the stringent Darwin instrument requirements. The soft material is cryogenically compatible and did not show degradations during the gamma radiation test. Multilayer AR-coatings have been developed and successfully tested. A proper cladding mode absorbing layer is available as well. A CCN is planned to implement silver halide as a material for the shorter wavelengths used in Darwin.

Development of a Tilt Actuated Mirror

Thilo Schuldt, Martin Gohlke, Wolfgang Kronast, Bernhard Müller, Antwi Nimo, Ulrich Mescheder, Ulrich Johann, Dennis Weise, and Claus Braxmaier



An electrostatically actuated micromirror with a $3 \times 3 \text{ mm}^2$ surface area and a thickness of $100 \mu\text{m}$ has been designed and realized where the tilt movement of the mirror is provided by a torsional load of the mirror suspension. For layout optimization, 3D FEM simulations were carried out; measurements showed a torsion angle of $\pm 1.9 \text{ mrad}$ at a driving voltage of $U = 200 \text{ V}$. A new design and fabrication concept for the micromechanical device was developed, taking care of high mechanical stability, very low-noise performance and minimized piston effect (i. e. the requirement that under rotation of the mirror no significant z-movement of the reflection surface occurs). This design of a tilt-actuated micromirror has potential application for the space mission LISA where actuators with pm and nrad stability are required as part of the optical bench. This project is carried out in a cooperation with HTWG Konstanz and the University Furtwangen.

The planned space mission LISA (Laser Interferometer Space Antenna) will measure gravitational waves in the frequency band $30 \mu\text{Hz}$ to 1 Hz . It utilizes high-precision laser interferometry between spacecraft with a distance of about 5 million kilometers where a sensitivity of $\sim 10 \text{ pm}/\sqrt{\text{Hz}}$ in translation measurement and $\sim 20 \text{ nrad}/\sqrt{\text{Hz}}$ in tilt measurement is needed. Two actuated mirrors are part of the optical path of the scientific interferometric measurement, and therefore have to fulfill very stringent requirements with respect to translation and tilt. In case that the rotation point of the actuated mirror does not coincide with the point of incidence of the laser beam on its surface, a rotation of the mirror results in a parasitic translation movement (so-called piston effect, cf. figure 1). Our mirror design takes into account the LISA requirements, but generally represents a high-precision actuator for ground- and space based interferometry and even for commercial applications such as laser projection.

Design and Simulation of the Mirror

The basic concept of our mirror is shown in figure 2. It is a hybrid device consisting of a silicon chip manufactured from SOI (silicon on insulator) wafer

carrying the mirror and two fixed reference mirrors and a pyrex glass chip with the counter electrodes in an etched cavity building the air gap between electrode mirror plate and counter electrode. Both chips are adhesively bonded together. The mirror is suspended by two silicon beams, which are fixed at the silicon substrate and deformed torsionally to provide rotation of the mirror (these devices are called therefore torsional micro mirror). The mirror plate is electrically contacted with aluminum contacts on the silicon substrate.

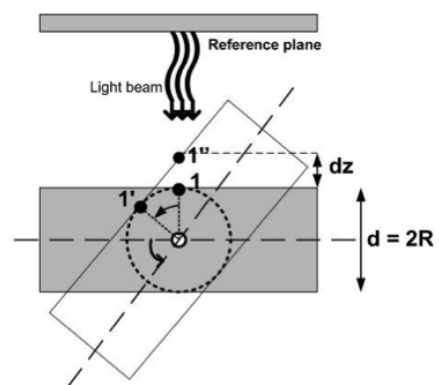


Figure 1: Schematic of the piston effect, here dz .

The active upper area of the mirror covers $3 \times 3 \text{ mm}^2$ surrounded by a stiffening frame of $100 \mu\text{m}$ thickness and $100 \mu\text{m}$ width, to give an additional

stabilization to the plate. The thickness of the mirror plate ($100\ \mu\text{m}$) and the additional stiffening frame around the mirror surface ensure a stiffness which guarantees the optical specifications and a flatness better than $\lambda/10$ rms.

An unintended z-displacement of the mirror surface under rotation and therefore the resulting change of optical path length are caused by two different effects: (i) movement of the whole mirror plate in the direction of the counter electrode under load caused by the electrostatic force due to finite stiffness of the beam based hinges; and (ii) movement of the mirror surface under rotation (piston-effect) in dependence of the position of the rotation axis.

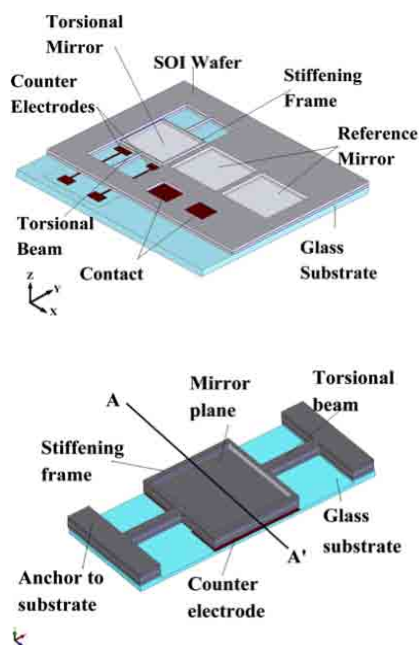


Figure 2: Schematic of the micromirror design. Implemented on the wafer are the tilt actuated mirror and two reference mirrors.

The first effect can be minimized by optimal choice of the geometrical parameters of the suspension beams, for example width, length and height of the beams. The torsional beams are chosen as small as possible in width to combine little z-displacement of the micromirror by the electric field from the counter electrode together with the possibility of easy rotation of the mirror at moderate voltages at the counter electrode. The second effect is minimized by a specific design where the rotational axis of the micromirror exactly coincides with the mir-

ror surface. This is achieved by using a symmetric SOI-wafer with handle and device wafer having exactly the same thickness. The reflecting plane of the mirror is formed by the handle wafer's surface. The suspending beams are realized from both, the handle and the device wafer of SOI-wafer. Thus the torsion axis of the beams coincides almost perfectly with the reflecting plane, the only difference is resulting from the small SiO₂-layer between handle and device layer which is in our case $2\ \mu\text{m}$ thick.

Functional Test

A first functional test of a prototype micromirror was carried out utilizing a Michelson type interferometer. The fringe patterns of the interferometric measurements are shown in figure 3 for different driving voltages. The measured rotations of the mirror are in good agreement with the theoretical values obtained by an FEM simulation using COM-SOL software.

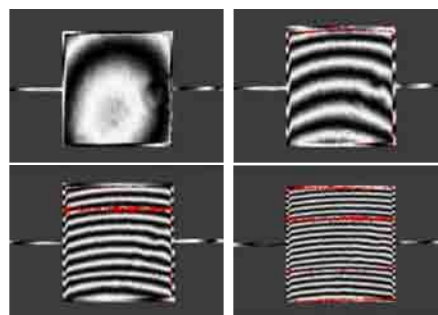


Figure 3: Photographs of the micromirror with applied driving voltages of 0 V, 100 V, 150 V and 200 V.

Outlook

In a next step, the prototype mirrors will be characterized using the high-performance interferometer which offers pm and nrad sensitivity. The rotational movement of the mirror will be measured as well as a possible z-movement. Static long-term measurements will be carried out for noise characterization.

This project is part of the work within the competence center (ZAFH) Photonⁿ financed by the state Baden-Württemberg, the Landesstiftung Baden-Württemberg and the European Union under EFRE.

Space Time Asymmetry Research – STAR

Thilo Schuldt, Mohammed Allab, and Claus Braxmaier



STAR is a proposed satellite mission that aims for significantly improved tests of fundamental space-time symmetry and the foundations of special and general relativity. In total, STAR comprises a series of three subsequent missions where STAR-1 will measure the constancy of the speed of light to one part in 10^{17} and derive the Kennedy Thorndike (KT) coefficient of the Mansouri-Sexl test theory to $7 \cdot 10^{-10}$. The KT experiment will be performed by comparison of an atomic standard with a highly stable cavity made from ultra-low expansion (ULE) ceramics. With an orbital velocity of 7.4 km/s the sensitivity to a boost dependent violation of Lorentz invariance as modeled by the KT term in the Mansouri-Sexl test theory or a Lorentz violating extension of the standard model (SME) will be significantly enhanced as compared to Earth based experiments. The low noise space environment will additionally enhance the measurement precision such that an overall improvement by a factor of 100 over current Earth based experiments is expected.

Lorentz invariance is one of the foundations of modern physics and was subject to experimental tests for 130 years. Historic tests can be subdivided into Michelson-Morley (MM) type experiments which look for directional violations of special relativity, and Kennedy-Thorndike (KT) type experiments which look for velocity dependent violations. In the Robertson-Mansouri-Sexl (RMS) test theory, the speed of light as a function of θ (the angle between the velocity vector and the direction of light propagation) and the velocity v (relative to a preferred frame, usually the cosmic microwave background, CMB) is given by

$$\frac{c(v, \theta)}{c} = 1 + (\beta - \epsilon - 1) \frac{v^2}{c^2} + \left(\frac{1}{2} - \beta + \delta\right) \frac{v^2}{c^2} \sin^2 \theta,$$

where β is the Lorentz contraction parameter, ϵ is the time dilation parameter, and δ the transverse contraction. According to special relativity, the last two terms on the right side are zero. In the RMS model, an MM experiment measures the amplitude of the θ -dependent term while a KT experiment measures the amplitude of the θ -independent term.

While the currently most accurate tests were carried out in ground-based experiments [1–4], space environment offers the opportunity of an optimization of parameters such as orbit time and change in velocity – and therefore a further improvement

in accuracy down to the 10^{-19} level. The lack of vibrations, acoustic and seismic noise in space enables long integration times and higher signal to noise ratios. A schematic of the STAR-1 satellite is shown in figure 1 where the relevant velocities are given: a velocity of 370 km/s of the sun-system relative to the CMB, an orbit velocity of the satellite of 7.4 km/s and an orbit time of 102 min.



Figure 1: Schematic of the STAR satellite.

The STAR project is a cooperative effort of NASA Ames Research Center (USA), Stanford University (USA), King Abdulaziz City of Science and Technology (KACST, Saudi-Arabia), Birmingham University (UK), the German space agency DLR, the Center for Applied Space Technology and Microgravity ZARM (Bremen), the Humboldt-University Berlin and the University of Applied Sciences (HTWG) Konstanz. STAR consists of a series of 3 missions with progressively advanced instrumentation.

The STAR-1 mission is meant to be realized ‘as soon as possible’, ‘as simple as possible’ – and therefore ‘as cheap as possible’. It will utilize state-of-the-art technology with proven performance at least in laboratory experiments. The STAR-1 payload will include a cavity stabilized laser (length standard), an atomic standard, an optical beat measurement unit, and a laser system. All subsystems will be realized twice for redundancy. A comparison of a length standard to an atomic standard will yield to a Kennedy-Thorndike experiment while a comparison of two length standards (orientated perpendicularly to each other) will yield to a Michelson-Morley experiment.

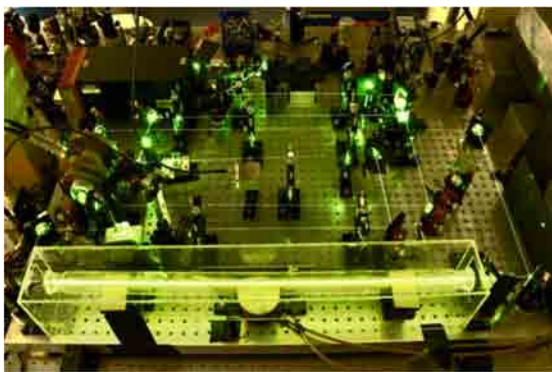


Figure 2: Laboratory setup of an Iodine standard.

The HTWG Konstanz and the Humboldt-University Berlin will realize an iodine standard based on modulation transfer spectroscopy (MTS) using strong absorptions of molecular iodine near 532 nm. The laser source is a Nd:YAG laser (non-planar ring oscillator design) at 1064 nm which is frequency doubled using a periodically poled KTP crystal. For achieving high mechanical stability of the optical setup, the baseplate is assumed to be made from Zerodur, a glass ceramics with a very low coefficient of thermal expansion of $2 \cdot 10^{-8} \text{ K}^{-1}$. The optical components will be fixed to the baseplate using adhesive bonding. The high mechanical stability ensures, that the optical alignment will survive vibrations during launch and also minimizes pointing variations of pump and probe beam relative to each other which otherwise limit the achieved frequency stability in the long term region. A photograph of a laboratory setup realized at the Humboldt-University Berlin is shown in figure 2. A frequency stability below $1 \cdot 10^{-14}$ at integration times of 100 s was demonstrated. The assembly-

integration technology of adhesive bonding is investigated in a current activity at HTWG Konstanz and EADS Astrium (Friedrichshafen), cf. the article by Thorsten Meisner.

The cavity laser stabilization, which is developed by Stanford University, will be based on a monolithic crossed cavity with 2 cavities perpendicular to each other, as shown in figure 3. The cavity spacer will be made of a material with very low coefficient of thermal expansion such as ULE or fused silica. For frequency stabilization, the method of Pound-Drever-Hall will be utilized.

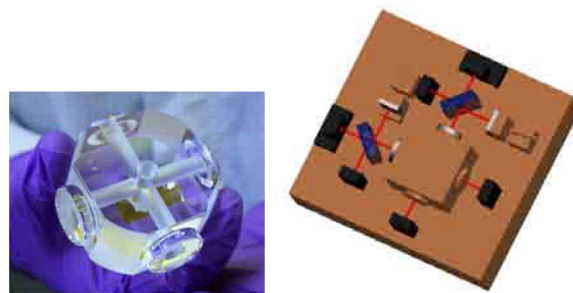


Figure 3: Left: photograph of a crossed cavity made of fused silica; Right: CAD schematic of an optical setup for laser frequency stabilization to an optical cavity.

Bibliography

- [1] C. Braxmaier, H. Muller, O. Pradl, J. Mlynek, and A. Peters. Test of relativity using a cryogenic optical resonator. *Phys. Rev. Lett.*, 88:010401, 2002.
- [2] S. Herrmann, A. Senger, K. Mohle, M. Nagel, E. V. Kovalchuk, and A. Peters. Rotating optical cavity experiment testing Lorentz invariance at the 10^{-17} level. *Phys. Rev. D*, 80:105011, 2009.
- [3] C. Eisele, A. Y. Nevsky, and S. Schiller. Laboratory test of the isotropy of light propagation at the 10^{-17} level. *Phys. Rev. Lett.*, 103:090401, 2009.
- [4] M. E. Tobar, P. Wolf, S. Bize, G. Santarelli, and V. Flambaum. Testing Local Lorentz and Position Invariance and Variation of Fundamental Constants by searching the Derivative of the Comparison Frequency Between a Cryogenic Sapphire Oscillator and Hydrogen Maser. *Phys. Rev. D*, 81:022003, 2010.

High Resolution Optical Profilometry

Ruven Spannagel, Marcell Liebhart, Walter Baumgartner, Thilo Schuldt, and Claus Braxmaier



In this report we present the current status of our high-precision profilometer. As a basis for the measurement setup a heterodyne interferometer is used and enables a non-tactile and high-precision surface property measurement. To detect the surface topology, the scanning of a surface is necessary. Therefore, we actuate the measurement beam. With our new design of the beam actuation system, we are able to achieve translation measurements with $900 \text{ pm}/\sqrt{\text{Hz}}$ -sensitivity below 200 mHz.

As the actuation of the laser beam should have no or minimum influence on the result, it is necessary that the length of the optical beam path through the full range theoretically remains constant ($\Delta Z=0$). For this purpose, we actuate a dove-prism for each translation axis by using a high precision nano xy-piezo stage. The schematic of the symmetric interferometer and the two dove-prisms are shown in figure 1.

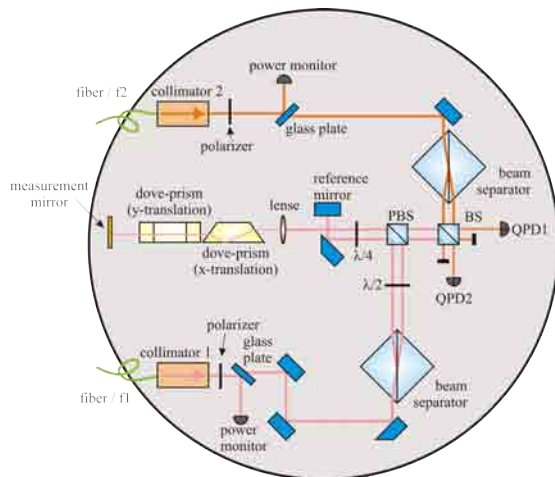


Figure 1: Schematic of the heterodyne interferometer setup and the two dove-prisms for beam actuation

The measurement facility which actuates the beam is shown in figure 2. The lightweight aluminum construction has a favorable vibration be-

havior to minimize the vibrations. The material for the mechanical components have a similar coefficient of thermal expansion as the optical components to reduce additional stresses due to temperature fluctuations. The piezo and the two prisms are mounted with clamps which are adjustable in three degrees of freedom. Therefore we are able to align the beam very precise.



Figure 2: Construction of the beam actuation system

The measured surface of a high-reflective mirror with a flatness of $\lambda/10$ is shown in figure 3. We scanned a square of $400 \mu\text{m}$ with 10 000 single measurements.

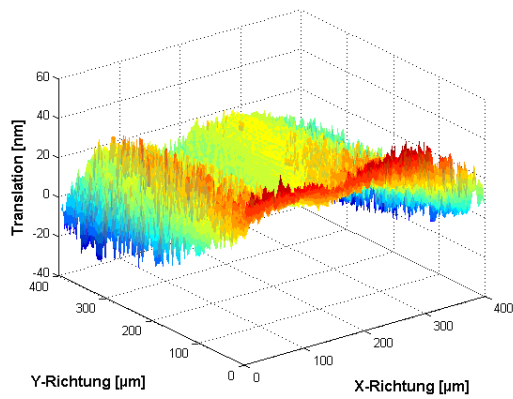


Figure 3: 3D profile of a $400\ \mu\text{m} \times 400\ \mu\text{m}$ surface

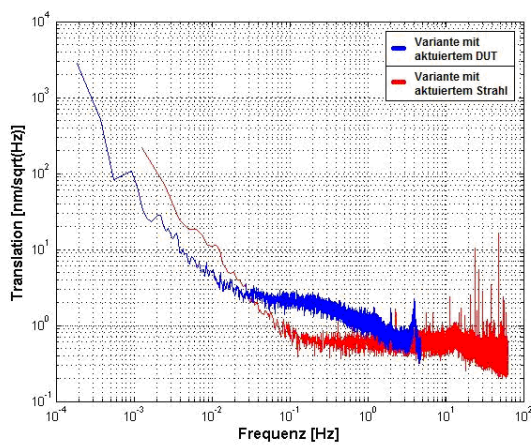


Figure 4: Power spectral density of a 40h noise measurement

The power spectral density (PSD) shows the sensitivity of our profilometer (cf. figure 4). The blue line corresponds to old DUT (device under test) actuating system and the red one to the new designed beam actuating system. With the beam actuation we could achieve a noise level of $900\ \text{pm}/\sqrt{\text{Hz}}$ for frequencies above 100 MHz. The lines also shows, that we could increase the sensitivity of our profilometer at a frequency of 0.2 Hz from 2 nm up to 900 pm.

Bibliography

- [1] Walter Baumgartner and Marcel Liebhart. Konzeption, Design und Realisierung einer Messstrahlaktuation für die höchstauflösende optische Profilometrie. Master Projekt HTWG Konstanz, 2009.
- [2] Ruven Spannagel. Integration und Test der Aktorik für ein Laserinterferometer zur hochauflösenden optischen Profilometrie. Bachelor Thesis HTWG Konstanz, 2009.
- [3] T. Schuldt, M. Gohlke, R. Spannagel, S. Resel, D. Weise, U. Johann, and C. Braxmaier. Sub-Nanometer Heterodyne Interferometry and Its Application in Dilatometry and Industrial Metrology. *International Journal of Optomechatronics*, 3(3):187–200, 2009.

3D-Digitization Using Fringe Projection and HDR Methods

Stefan Jacob and Claus Braxmaier



Scanning of shiny or reflective metal surfaces using structured light methods is particular challenging. As a shiny object in general can not be lit from single exposures with fixed shutter speed, a procedure which combines different series of exposures with different exposure times to series with high dynamics is obviously a solution with the restriction of a non moving scene. Exposing an object with different duration periods (exposure times) data can be obtained from very shiny or bright areas of an object by choosing very short exposure times for highly reflective parts of the object which minimizes irradiation effects on that parts. The non - bright area of the object is illuminated, however, no longer optimal in general. The combination of multiple exposure times so that all possible areas of the object to be scanned at least have in minimum one optimal lighting in one of the acquisition series images should therefore result in an improvement in the data situation. Since current CCD cameras also tend to show a strong noise in the captured images the combination of several images should also counteract this.

Assuming a linear camera response curve a HDR (high dynamic range) image is calculated for each strip from the available image frames in each case in form of a 32bit floating point image. The individual pixels are normalized on the shutter time and the gains that were used for each recording, and then a weighted average is calculated. The weighting is realized via a "sawtooth function" which, starting from zero, in the interval between a lower and upper threshold value increases linearly and then falls back to zero.

$$g_{HDR} = \frac{\sum_{i=0}^N \frac{w(g_{i,x,y}) \cdot shutter_{max} \cdot gain_{max}}{shutter_i \cdot gain_i}}{\sum_{i=0}^N w(g_{i,x,y})},$$

$$\forall x = [1..imagewidth] y = [1..imageheight]$$

The parameterization of the lower and upper threshold thus permits a direct influence on the confidence level of the camera response curve, that means the range between upper and lower threshold defines the area of the camera response curve, which can be assumed to be linear and therefore used for data retrieval.

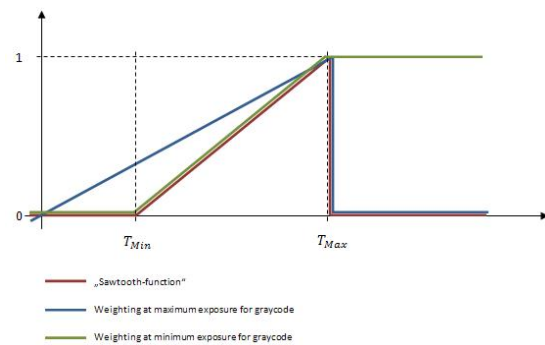


Figure 1: Weighting function used for HDR calculation.

For the calculation of gray code images a similar procedure is used, but here the whole data range provided by the input images is used, that means for the "darkest" record (longest shutter time), the lower threshold is automatically set to 0, and for the "brightest" record (shortest shutter time) values above the upper threshold value are weighted with 1. This means that in the resulting graycode fewer "holes" are created, which would occur if one would weight pixels outside the region (lower/upper threshold) with zero as done in the calculation of the stripe images.

The process resulting from the combination of several shots with a data range of 8bit per pixel, leads to resulting data with larger areas. To create the conditions for the mapping of high dynamic

images, data areas must therefore be realized that map to fractional numbers in a sufficient accuracy. As format for the results therefore a type of images was chosen, which uses 32 bits per pixel data width, shown in the float data format, was selected (in addition 32bit floating point image). The potential for realization of export and import capabilities for such data and the possibility of visualization of these on the monitor were also examined and exemplarily integrated.

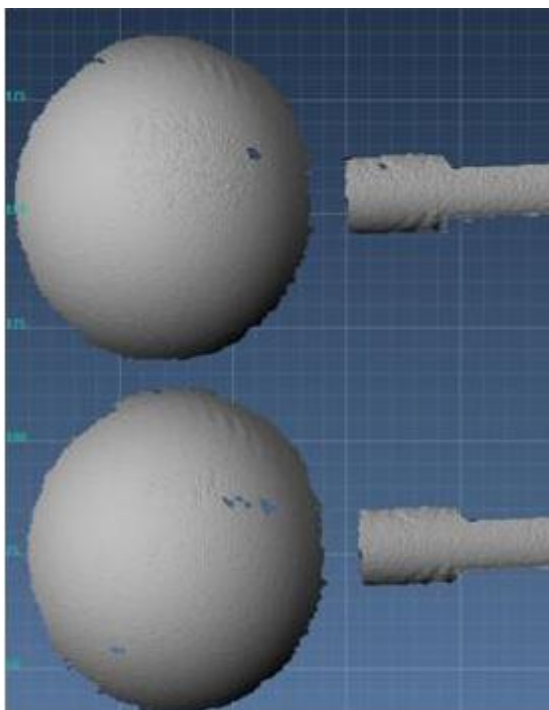


Figure 2: Comparison of scan data of a dumbbell with 1.4 megapixel cameras without (above) and with (below) using the HDR technique.

To examine the results, data was generated with the already available "1fromN" process and the new HDR process and the resulting 3D data sets were compared. As a result a significant reduction of ar-

tifact formation at bright spots as well as an obviously noise reduction can be reached.

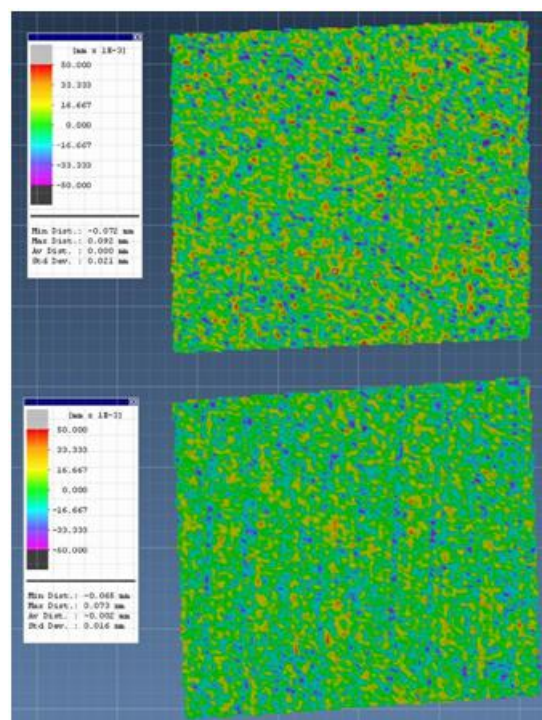


Figure 3: Comparison of noise reduction results on scan data of a plane object without (above) and with (below) using the HDR technique.

The next challenging task within the scope of this project is speeding up the whole process. As in some cases 3d data quality is the biggest concern, in other applications it is speed that counts. So called "handheld scanners" are desirable, when either there is no way of using a tripod or when the object itself is moving or deforming so quickly that short acquisition times are a must. With high speed cameras at 120Hz framerates and a projector of the same speed, scanning times of below 0.1s are possible now. Available resolution will be only VGA (640x480) though.

Preparation of the 'Fertigungs-Messtechnik 2' Laboratory

Mohammed Allab, Karl-Heinz Waller, Tobias Pitzner, Sebastian Voigt, and Claus Braxmaier



During the next winter term 2010/2011 a new laboratory is going to take place within the framework of the course "Production Measurement Technology 2". The main objective of this laboratory is that the students learn the principles of modern optical measurement techniques using a commercial fringe projection system by Breuckmann GmbH. The students learn the basics of optical measurement systems and their prospects in hands-on experiments. For that purpose a comparison between optical and tactile measurement systems will be performed where students have to digitize a defined test specimen using the SmartScan 3D system by Breuckmann GmbH. After that they are going to measure the obtained scatter plot with the controlling software "Qualify" of Geomagic Company. The test specimen will be remeasured by the students using the 3D coordinate-measurement machine (CMM) by Mitutoyo. The students are going to compare the measurement results and to analyze the deviations at home.

The laboratory uses a commercial 3D digitization system by Breuckmann GmbH (Meersburg). This system consists of a measurement head consisting of a projector and two cameras, an electronics unit and a host computer. A series of equidistant stripes (using Graycode and phaseshift light projection) is projected on the test specimen and stereoscopically recorded by the two cameras. A photograph of the setup is shown in figure 1.

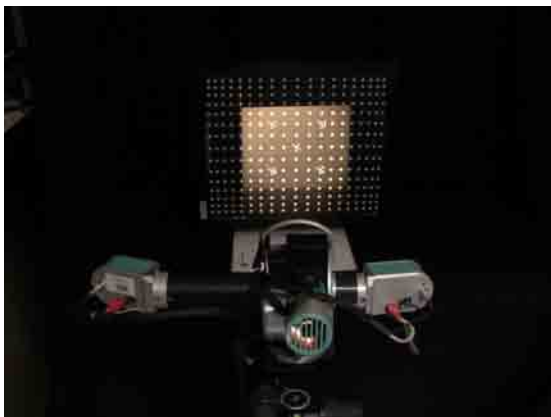


Figure 1: Photograph of the Breuckmann stripe projection system with calibration plate.

The laboratory practice is executed as follows:

1. 3D digitization of a test specimen using index marker method. Therefore so-called index marks are fixed to the test piece which

are used to recombine the obtained 3D scatter cloud data appropriately.

- a. Installation of the test specimen and the digitizing system.
 - b. Performance of a scanning process using the scanning software Optocat 2007.
 - c. Knowledge of the theoretical and technical basics.
2. Evaluation process using the Software 'Qualify' by Geomagic
 - a. Getting familiar with the software.
 - b. Alignment and dimensioning of the obtained scatter cloud data.
 - c. Preparation of a test report.
 3. Tactile measurement of the test specimen using the CMM by Mitutoyo.
 - a. Handling of the CMM.
 - b. Data evaluation.
 4. Analysis of data and report
 - a. Comparison of the obtained data sets (optical scan and CMM measurement).
 - b. Preparation of a laboratory report.

- c. Evaluation of the reasons for a possible deviation and the principles of measurement.

For this laboratory, first two test specimens were defined and procured. These specimens can be scanned using the optical 3D digitization system as well as the tactile CMM. The inspection software was acquired and implemented. For instructing the students carrying out this laboratory in their studies, a new method was realized. In addition to the common laboratory notes, where the students can e.g. find the handling regulations of the applications, also some introductory videos can be found which explain the requested information in a visual and acoustic way to the students. Therefore, we expect a better preparation of the students in the preliminary stage of the practice part.

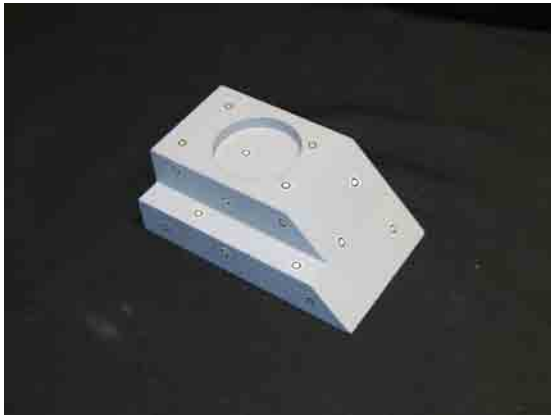


Figure 2: Test specimen with index marks.

The optical digitization system is now in working condition, the instruction videos are realized and the colleagues are familiarized with the SmartScan 3D system. Before the laboratory starts, following issues have to be done:

1. Preparation of the test specimen:
 - Varnish the test specimen (in order to avoid reflections during the scanning process)
 - Create reference data sets using the CMM and SmartScan
2. Field experiment carried out by students

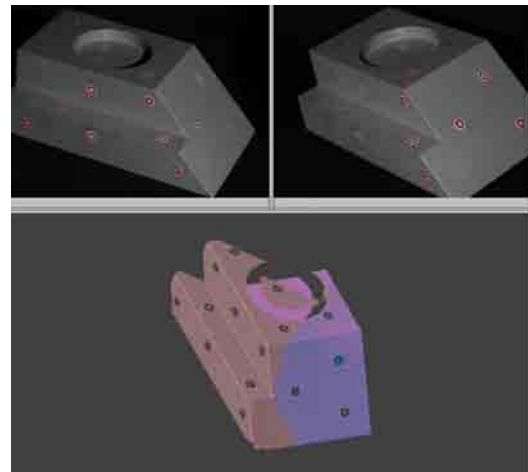


Figure 3: Test specimen and scatter cloud data.

What a Plant Sounds Like: The Statistics of Vegetation Echoes as Received by Echolocating Bats

Matthias O. Franz, Yossi Yovel¹, Peter Stilz², Arjan Boonman³, and Hans-Ulrich Schnitzler²



Bats are able to recognize complex object classes from ultrasound signals alone. So far it has been elusive which signal features form the base of the astonishing sensory capabilities of these animals. We use modern methods of machine learning [1] and sensory statistics of ultrasound echoes [2] to systematically analyse a large number of candidate ultrasound features and to evaluate their relevance for the underlying decision process. This methodology was applied to an important type of bat behaviour: the recognition of plant species from their ultrasound echoes.



Figure 1: A bat hunting for prey must be able to discriminate its ultrasound signature from the complex background of vegetation echoes.

More than 800 species of bats perceive their surroundings through echolocation. They emit ultrasonic pulses and analyze the information conveyed in the echoes returning from objects in their surroundings. This enables bats to orient in space, to acquire food and to perfectly function in complete darkness. In the absence of light, echoes constitute a major part of the sensory world of bats. Understanding their characteristics can thus help to shed light on the echolocation sensory system.

¹Department of Neurobiology, Weizmann Institute of Science, Rehovot 76100 Israel

²Animal Physiology Department, University of Tübingen

³INCM-CNRS UMR, Marseille, France

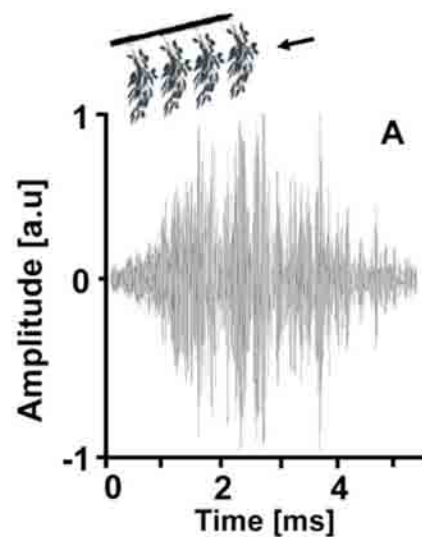


Figure 2: Example of a complex vegetation echo created from a branch with four twigs. The twigs show up in the echo as four amplitude maxima.

A critical step on the way to understanding a sensory system is the analysis of the input it receives. We examined the statistics of natural complex echoes, focusing on vegetation echoes [2]. Vegetation echoes constitute a major part of the sensory world of echolocating bats and play an important role in several of their daily tasks. Our sta-

tistical analysis was based on a large collection of plant echoes acquired by a biomimetic sonar system. We explored the relation between the physical world (the structure of the plant) and the characteristics of its echo. Finally, we completed the story by analyzing the effect of the sensory processing of both the echolocation and the auditory systems on the echoes and interpreted them in the light of information maximization.

The echoes of all different plant species we examined share a surprisingly robust pattern that was also reproduced by a simple Poisson model of the spatial reflector arrangement. The fine differences observed between the echoes of different plant species can be explained by the spatial characteristics of the plants. The bat's emitted signal enhances the most informative spatial frequency range where the species-specific information is large. The

auditory system filtering affects the echoes in a similar way, thus enhancing the most informative spatial frequency range even more.

Bibliography

- [1] Y. Yovel, M. O. Franz, P. Stilz, and H.-U. Schnitzler. Plant classification from bat-like echolocation signals. *PLoS Comput. Biol.*, 4(3):e1000032. doi:10.1371/journal.pcbi.1000032, 2008.
- [2] Y. Yovel, P. Stilz, M. O. Franz, A. Boonman, and H.-U. Schnitzler. What a plant sound like: the statistics of vegetation echoes as received by echolocating bats. *PLoS Comput. Biol.*, 5(7):e1000429. doi:10.1371/journal.pcbi.1000429, 2009.

Steganalysis Using Stochastic Image Models

Le Pham Hai Dang, and Matthias O. Franz



The quantity and the variety of steganography methods complicate the detection of secret messages in digital images. In order to handle all of these embedding methods, the detection of steganograms (images with embedded messages) should be independent of the embedding method. The main focus of our work is on creating a universal blind steganalytic algorithm based on a previously developed predictive image model [1].

Two approaches form the semantic field of security: cryptography and steganography. Although both disciplines aim at information security, cryptography stands in the first place for the protection of the contents of the message. One problem with cryptography still holds: the presence of a secret message is obvious. In contrast, steganography is concerned with hiding the secret message. From this perspective, the process of steganography needs a cover (image, mp3, ...) wherein the secret message is to be embedded (Fig. 2). In our example, both the cover and the secret message are images (Fig. 1(a) & Fig. 1(b)).



(a) Cover

(b) Message

Figure 1: The Monet Water Lilies (1906) [2] and satellite photo of the suspected uranium enrichment site in Iran (Reuters)

The countertechnology to steganography is called *steganalysis*. This discipline is concerned with the detection of steganography (Fig. 3). Steganalysis without knowing the specific method of steganographic manipulation is called *universal* or *blind Steganalysis*. In our approach we regard the detection problem of steganalysis as a binary classification problem. As classifier we use modern learning machines, the so-called *Support Vector Machines (SVMs)* [3].

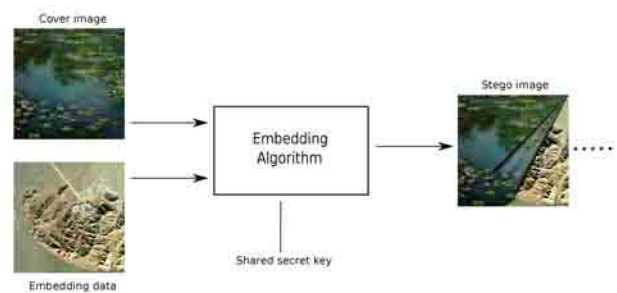


Figure 2: Steganography: a secret message is embedded into a cover such that it cannot be noticed by an unsuspecting observer.

These machines need descriptive image features that capture the relevant characteristics of the image and allow for an efficient discrimination between clean and stego images.

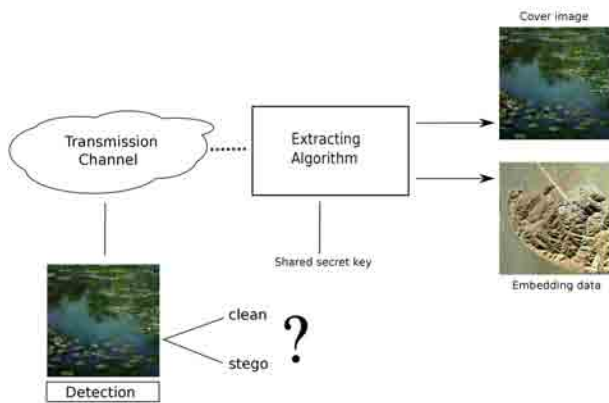


Figure 3: Steganalysis: detection of the presence of a secret message in the cover.

Image pixels, as substructure of images, are strongly correlated with their neighbourhood pixels and therefore can be largely predicted. In this study, neighbourhood relations are captured in an image model that predicts the grayvalue of every pixel from its surrounding neighbours. The steganography embedding process destroys the strong correlation between image pixels. Thereby the value of the predicted image pixels changes so far that this

difference between clean and stego images can be recognized by measuring the statistical moments (mean, variance, etc.) of the pixel distribution. These moments form the relevant characteristics of the image that serve as input for the SVM classifier.

Acknowledgments. The author would like to thank Andrew P. Smith and Markus Meßmer.

Bibliography

- [1] M.O. Franz and B. Schölkopf. Implicit wiener series for higher-order image analysis. volume 17, pages 465–472, Cambridge, MA, USA, 2005. MIT Press.
- [2] <http://www.ibiblio.org/wm/paint/auth/monet/waterlilies/>.
- [3] Bernhard Schölkopf and Alexander J. Smola. *Learning with Kernels. Support Vector Machines, Regularization, Optimization, and Beyond*. The MIT Press, Cambridge, MA, USA, 2002.

The *Optical Radar* - a Multidisciplinary Research Project

Jürgen Keppler and Matthias O. Franz



The goal of this project is to overcome the problem of inertia in optical telescopes by using a rotating mirror optics instead of moving the entire telescope. The mirror rotates at a constant rate. Whenever it reaches the desired rotation angle, the exposure of a new image is triggered. By changing the timing of the trigger signal, arbitrary azimuthal viewing directions can be chosen at a very high speed.

The first problem to be settled is that of *motion blur* (Fig. 1). We currently investigate various image restoration techniques with respect to their capabilities for our purpose. Most of these techniques profit considerably from knowing the exact movement of the mirror. In our setup, rotation rate is measured by a set of Hall effect sensors. Whether these sensors are already sufficient for deblurring or whether additional image-based estimation techniques are necessary, is subject of a recently started master thesis.



Figure 1: The rapidly rotating mirror optics leads to motion blur in the recorded images.

Independent of the used deblurring technique, motion blur should be kept as small as possible. We therefore use a Peltier-cooled camera that allows for small exposure times while maintaining a high frame rate of 30 images per second.

The second problem we face is the design of the experimental setup (Fig. 2) which has to be stable under the dynamical stress created by the rapidly rotating mirror. The mirror is mounted with brackets on slewing rings which are driven by an electric motor. The optical axis of the camera system must be aligned exactly at the rotation axis. A mount which is adjustable in four degrees of freedom is necessary for this. The mount consists of two orthogonal linear stages and two goniometers. The calibration procedure for the mount is developed in another diploma thesis (see project description S. Lang, "Calibration of the Sensor axis").

The third challenge lies in the mirror brackets. We aim at a rotation speed of 1800 rpm. The arising rotation forces must be caught by the brackets, so that the mirror cannot fly away. The construction of the brackets is subject of a student project in mechanical engineering (see project description A. Winter and M. Repp, "A bracket for a rapidly rotating mirror").

The fourth subproject, the control of the electric drive and the evaluation of the sensors is done with a standard PC. The control has to be real-time, because the exposure must be triggered at the right moment. The electric drive already has an integrated control which allows for an independent control of the rotation rate.



Figure 2: Experimental setup.

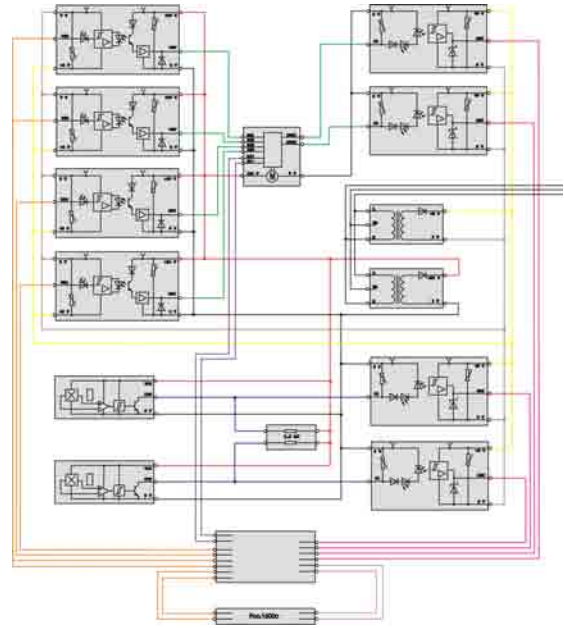


Figure 3: circuit design

Bibliography

- [1] Azriel Rosenfeld and Avinash C. Kak. *Digital Picture Processing*, volume 1. Academic Press, New York, 2 nd edition, 1982.

A Bracket for a Rapidly Rotating Mirror

Markus Repp, Alexander Winter, Jürgen Keppler, and Claus Braxmaier



The function of the *Optical Radar* is to monitor the surrounding area at a very high resolution and speed. Therefore a mirror is placed on the optical axis of a camera. By rotating the mirror it is possible to observe all azimuthal directions. The challenge for the device and especially for the bracket construction is the high rotational speed of maximally 1800 revolutions per minute. The rotational speed creates large forces and moments. We tried to keep these forces small by using aluminum as the key material in the construction.

The result of rotational motion is a centrifugal force. The centrifugal acceleration is defined as

$$a = \omega^2 \cdot R$$

With Newton's second law

$$F = m \cdot a$$

we obtain the formula for the centrifugal force as

$$F_c = \omega^2 \cdot R \cdot m.$$

The relation between centrifugal force, radius and rotation speed is graphically depicted in Fig. 1.

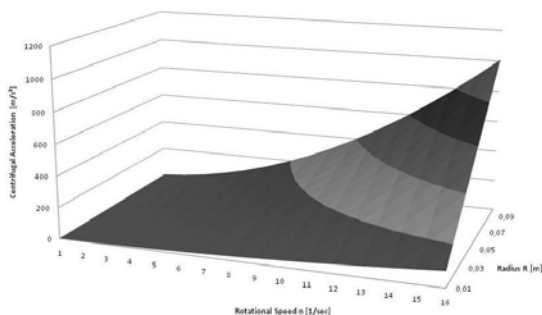


Figure 1: Centrifugal force depending on radius and rotational speed

Because the system requires 1800 rpm, there are only two possibilities to keep the centrifugal force small. One possibility is the use of lightweight materials, the other the skillful design of the bracket.

Both possibilities are based on the idea to save weight.

In case of the material we decided to use aluminum for the brackets. There are several reasons for using aluminum. In comparison to steel, it is much more lightweight and has almost the same mechanical strength. Furthermore it is easy to manufacture aluminum. Our first design of the brackets is shown in Fig. 2.

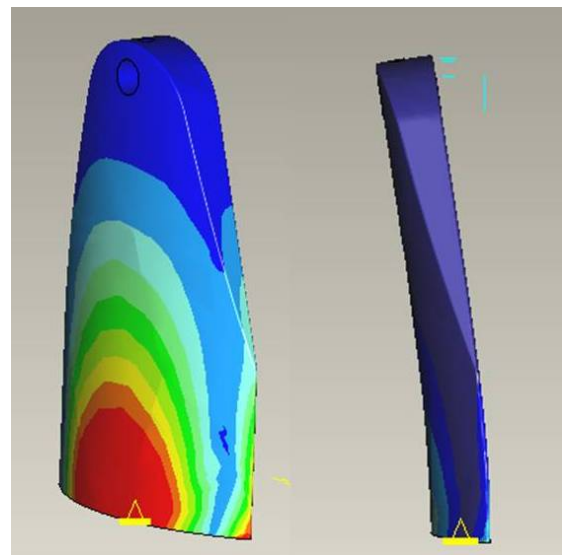


Figure 2: Left: Tensions from centrifugal force; right: Displacement

With the CAD software ProE we calculated the arising forces. Fig. 2 shows that our first construc-

tion had troubles at the bottom with some really high tensions. The centrifugal forces also created displacements of the brackets. We solved this problem through connecting the two brackets with a rod as shown in Fig. 3.

The next step in the construction was the adding of the mirror and the further enhancement of the brackets. The mirror should be replaceable and the angle of the mirror adjustable. Therefore we placed the mirror in a holder of aluminum.

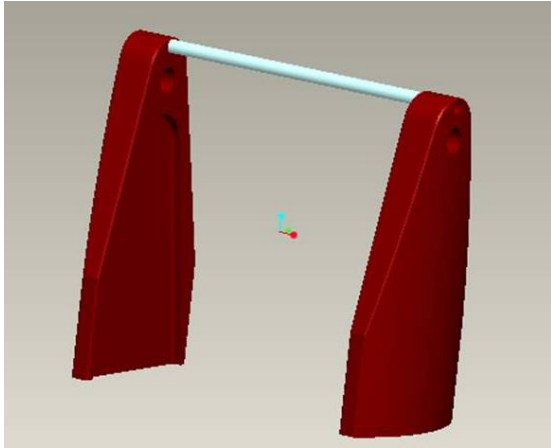


Figure 3: Brackets with rod

The final design is shown in Fig. 4. Because the

mirror is attached with a tilt angle, some weight is outside of the fulcrum. This causes additional centrifugal forces and torsion moments. The torsion moments stress the connection between bracket and holder. To absorb this moment, we extended the diameter of the connection.



Figure 4: Final construction

Calibration of the Sensor Axis

Stefan Lang, Jürgen Keppler, and Matthias O. Franz



The *Optical Radar* (see project description by J. Keppler) consists of a rotating mirror and camera optics. Both the rotation axis and the optical axis must be aligned in a calibration process. In this project we develop an image-based method for determining the position and orientation of the rotation axis. Also the principal point of the camera as part of the inner orientation is determined.

In the *Optical Radar*, objects seen at a given elevation angle should have a common radial distance to the principal point in the camera image. This simplifies the subsequent processing of the camera images considerably. In order to achieve such a geometry, a calibration procedure is needed to align the rotation axis with the optical axis of the camera. During operation, the opto-mechanical parts of the *Optical Radar* are liable to variations due to temperature changes and mechanical stress. As a consequence, the calibration procedure has to be repeated from time to time, preferably in place and with small effort.

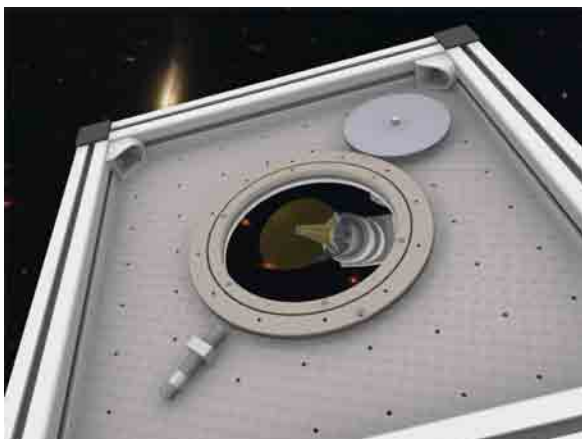


Figure 1: A circle appears to be an ellipse if the rotation axis of the slewing rings and the optical axis of the camera not aligned.

The camera is mounted in the experimental setup such that it can be regulated in four degrees of freedom. The mount is a combination of two precision linear stages and a Theta-Phi-Goniometer. In the first initialization of the setup, we can adjust the optical axis of the camera manually, but with low precision. In the next step, a small visual marker (e.g. a board with a small hole) is mounted on the slewing rings such that it rotates with the mirror.

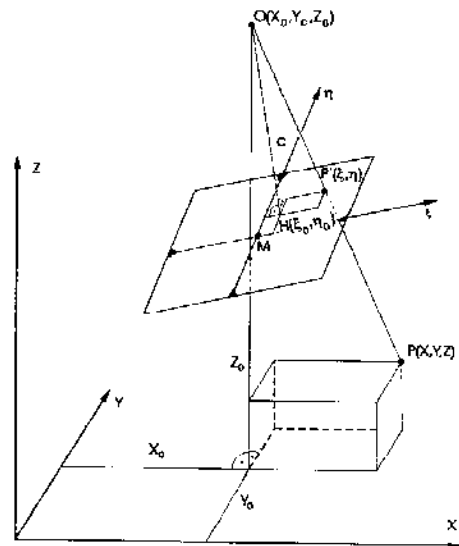


Figure 2: An object consisting of markers with known position can be used to find the inner orientation parameters of the camera (mainly focal length and principal point) from the laws of perspective projection [1].

The rotating ring with the marker describes a curve on the camera image. If the rotation axis and the optical axis of the camera are perfectly aligned, a sensor image with a large exposure time shows a perfect circle, otherwise the image contains an ellipse or part of an ellipse. This image is used to calculate the ellipse parameters. Because we know the parameters of the experimental setup and the ellipse, we can now calculate the adjustments that have to be made at the goniometer and the linear stages. This step can be repeated until the desired precision is reached.

The principal point of the camera is determined in another calibration procedure before it is installed in the experimental setup. Standard photogrammetric methods as described in [1] are used to compute the inner camera orientation parameters which include the principal point. The procedure requires at least two images of a calibration object, taken from two different positions. The calibration object contains simple markers which are known in size and distance to each other.

Bibliography

- [1] Karl Kraus. *Photogrammetrie, Band 1, Geometrische Informationen aus Photographien und Laserscanneraufnahmen*. Walter de Gruyter Verlag, Berlin, 7 edition, 2004.
- [2] Jürgen Bollmann. *Lexikon der Kartografie und Geomatik*. Spektrum Akademischer Verlag, Heidelberg, 2002.
- [3] Walter Kreiling Jörg Albertz. *Photogrammetrisches Taschenbuch*. Herbert Wichmann, 4 edition, 2002.
- [4] Helmut Kager Karl Kraus, Josef Jansa. *Photogrammetrie, Band 2, Verfeinerte Methoden und Anwendungen*. Walter de Gruyter Verlag, Berlin, 1996.
- [5] Thomas Luhmann. *Nahbereichsphotogrammetrie, Grundlagen, Methoden und Anwendungen*. Herbert Wichmann Verlag, Heidelberg, 2000.

Removal of Complex Lens Distortions

Stefan Florschütz and Matthias O. Franz



Image distortion is an intrinsic trait of all object lenses. Technically it is an aberration, which causes normally straight lines to appear warped or crooked. This error is created by the locally varying magnification, resulting from the fact that the focal length is different for different image angles. For high-precision image processing it is therefore important to remove this lens distortion before continuing to work with the image.

The simplest and most common forms of distortion are radially symmetric distortions like *barrel*- and *pincushion*-distortion. Barrel distortion is characterized by a decreasing magnification towards the edges of the image, while pincushion distortion is recognizable from an increase in magnification towards the edge.

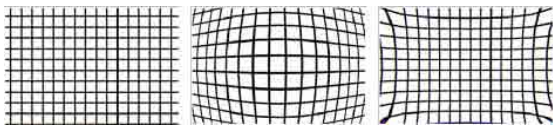


Figure 1: Effects of radially symmetric distortions. From left to right: *Distortion-free image*, *barrel distortion*, *pincushion distortion* [1]

In practice, it is often the case that different kinds of distortions are overlapping and thus creating a complex distortion pattern. Such complex distortions are not as easily removable as the radially symmetric ones.

Basically one has to extract and compute the distortion field, which contains informations about the degree and direction of the distortion at every position in the image. This field can then be used to remove the distortion from the image.



Figure 2: Left: Original image, right: distorted image using an exaggerated complex distortion field.

The method of acquisition of the aforementioned distortion field is the subject of this diploma thesis. An image of a known pattern of markers (*blobs*) is taken. Because of the lens distortion, the markers in the image do not correspond to the original pattern, i.e. distances between markers can be shorter or longer than in the original, or connecting lines between markers are not parallel or orthogonal.

The markers in the image are detected using an edge detection algorithm. It is essential to determine the centers of the markers as accurately as possible. This is achieved by use of the Zhou-Operator [2], which allows for sub-pixel positional accuracy.

Now that the relative distortion of the small number of markers is known, this information can be used to interpolate the distortion field at every pixel in the image. This is achieved by means of a training process using a Gaussian Process model [3]. The distortion field of the markers acts as input for the training process.

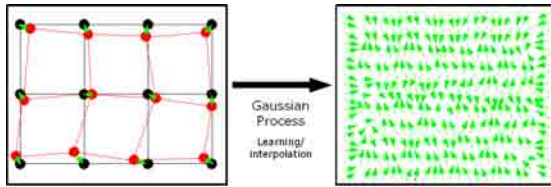


Figure 3: Removal of complex lens distortion. Left: original pattern (*black*), distorted pattern (*red*), rectification vectors for distorted markers(*green*). Right: sketch of trained distortion field. Note the rectification vectors across the whole image.

Bibliography

- [1] http://www.dxo.com/en/photo/dxo_optics_pro/optics_geometry_corrections/distortion.
- [2] Thomas Luhmann. *Nahbereichsphotogrammetrie - Grundlagen, Methoden und Anwendungen*. Wichmann, 2000.
- [3] C. E. Rasmussen and C. K. I. Williams. *Gaussian processes for machine learning*. MIT Press, Cambridge, MA, 2006.

Texture Continuation with Texture Synthesis and Inpainting

Stephan Seidel, Robert Massen, and Matthias O. Franz



Untreated natural wood panels are frequently contaminated and damaged, leading to the wood appearing aesthetically inferior. Currently, damaged regions of a panel is repaired manually. This is painstaking work and it's still possible to clearly see these repairs. A new idea is to paint over these imperfections with newly synthesized pieces of texture. The new texture is generated such that its characteristics as perceived by the human eye will be the same.

Texture synthesis is the process of constructing a new large texture image from a small digital input texture.

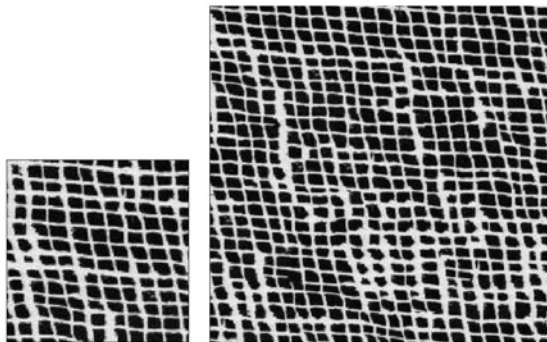


Figure 1: left: input image; right: synthetic image

Square patches from the input texture are stitched together to synthesize a new output image. This process of image quilting works similar to putting together a jigsaw puzzle. Certainly a random choice of patches is not satisfactory, because along the edges of structured texture patches it will be quite obvious that the patches do not match, and thus the texture will not appear uniform to the human eye.

A better method is to allow for a certain region of overlap between the patches. In this case, one searches for new patches whose appearance fits to its neighbors in the region of overlap. In the re-

gion of overlap, the patches are not simply averaged, but, before placing a chosen patch into the texture, one finds a boundary between the patches that minimizes an error function between the two patches. The boundaries between the single patches becomes thus invisible, and the created texture appears uniform. [1]

A second improvement is, instead of filling the texture in a fixed order, to find a fill order which continues a linear structure (isophote) such as the lines structures in a wood texture. Criminisi [2] describes a solution to this problem: one first selects the region in the image that one would like to replace, e.g., a damaged region in a wood panel. The rest of the image represents the input texture that has to be continued. All candidate patches for filling the target region are chosen from this input texture.

The fill order of the target region is controlled by a priority value. The priority P is defined as the product of two terms representing a balance between a confidence and a data term. The confidence term C represents the degree of match between a patch the surroundings of point p . The data term D is a function of the strength of isophotes intersecting the edges (point p) between the target region and the source region. As a result, patches with high confidence and sitting on prominent edges are more likely to be continued than others which leads to a natural continuation of edges over the target region (inpainting).

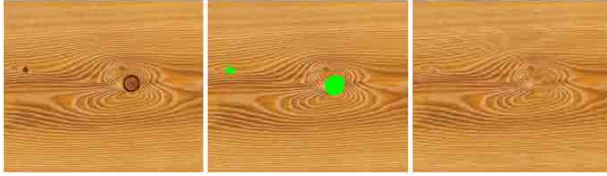


Figure 2: An example of removal. From left to right: original image, the damaged or unpleasing target region marked in green, result of region filling.

In our project, we apply these techniques for inpainting to untreated natural wood panels. In the final system, the target regions are detected automatically by standard surface inspection algorithms. The damaged regions are removed by CNC milling

tools and filled in with putty. For visually satisfying results, the recording colour camera and the printing device have to be calibrated carefully. We currently work in a simplified setting where the actual wooden surfaces are replaced by printouts of their recorded images.

Bibliography

- [1] Alexei A. Efros and William T. Freeman. Image quilting for texture synthesis and transfer, 2001.
- [2] Criminisi Erez Toyama, A. Criminisi, P. Pérez, and K. Toyama. Object removal by exemplar-based inpainting. pages 721–728, 2003.

Digital Image Steganography

Olga Schönemann, Markus Meßmer, Le Pham Hai Dang, and Matthias O. Franz



Steganography is the art of hidden storage or transmission of information. In contrast to cryptographic systems, which turn the message into an obscure encoded output, steganographic systems attempt to hide their existence by embedding them into an unobvious cover (images, mp3, etc.). Nowadays there are numerous steganography tools, like OutGuess [1], Steghide [2] or F5 [3]. Unfortunately, these applications have the disadvantage that they only support two or three image formats and only one or two algorithms, making a fair comparison more difficult. Therefore, the integration of additional algorithms is impossible.

In this project, we develop a steganography framework that avoids these disadvantages. The steganography system can be divided into three components (Fig. 1):

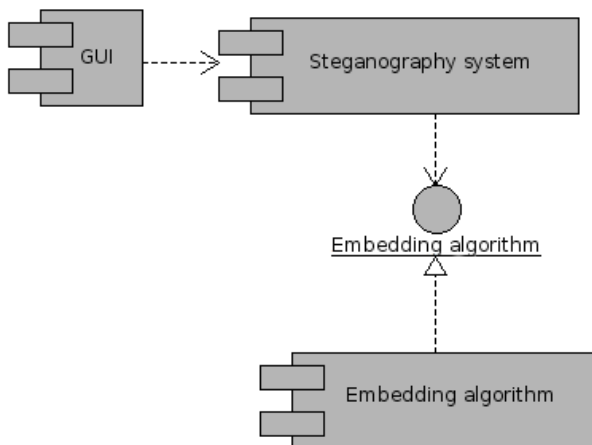


Figure 1: Steganography system

The system works in three steps. It first encrypts the file, then it opens the image and loads the library. In the last step the message is embedded in the image. In addition to embedding, the program supports the extraction of a message using various techniques, setting a target directory, the encryption of a file and the transfer of parameters required by the libraries.

The complete task of preprocessing is done by the steganography system, i.e. the library developers

only need to worry about the embedding or the extraction.

The current version includes three algorithms:

- LSB (Least Significant Bit)

A simple method which embeds into the bit planes of an image. For example: It uses the last bit of an 8 bit per pixel image (grayscale) and replaces it with one message-bit. [4]

- F5

F5 is an advanced method of JSTEG [3]. Instead of embedding in each pixel, the algorithm replaces randomly-selected pixels and uses matrix coding to reduce the number of pixels that have to be changed.

- Noise approach

This algorithm belongs to the adaptive techniques. Adaptive techniques respect the image contents during the embedding process. This means that the algorithm tries to simulate natural noise by changing bits only where the existing noise is high enough. [5]

By using the framework it is possible to integrate many more algorithms that can be used to embed in various image formats.

Bibliography

- [1] Jessica Fridrich, Miroslav Goljan, and Dorin Hoge. Attacking the outguess, 2002.
- [2] Stefan Hetzl. Steghide. <http://steghide.sourceforge.net/index.php>, 2003. (cited 2010/05/20).
- [3] Andreas Westfeld. F5-a steganographic algorithm. In *Information Hiding*, pages 289–302, 2001.
- [4] Sushil Jajodia Neil F. Johnson. Exploring steganography:seeing the unseen. In *Computing Practices*, pages 28–30, 1998.
- [5] Eiji Kawaguchi and Richard O. Eason. Principle and applications of bpcs-steganography, 1998.

Real-Time Multi-Camera Matching for 3D Reconstruction

Klaus Denker and Georg Umlauf



For multi-camera-based 3d reconstruction there is the trade-off between the quality of the computed depth map and the speed of the computations. Whereas high quality matching methods take several seconds or minutes to compute a depth map for one set of images, real-time methods achieve only low quality results.

Here we present a multi-camera matching method running in real-time for high resolution depth maps. It is based on a novel multi-level combination of normalized cross correlation, deformed matching windows based on the multi-level depth map information, and sub-pixel precise disparity maps. It is implemented completely on the GPU to process four 0.7 megapixel images in 10.5 milliseconds to a full resolution 3d depth map tailored to 3d face recognition.

Stereo matching is a techniques to compute from two or more 2d camera images a depth map of the captured object. It is used in remote sensing, robotics, archeology, cultural heritage, reverse engineering, and 3d face recognition [1, 2], because it is the only passive method to compute depth information. This means only natural light is used for the data acquisition without artificial interaction with the object that might harm it.

However, there is the trade-off between the depth map quality and the computation time. Where a real-time computation is not important the multi-view-matching methods focus on high quality results. These methods need at least several seconds to compute a single depth map from one set of images [3]. However, for robotics faster computation times are more important leading to GPU-based real-time matching methods [4].

Our target application is 3d face recognition, where the requirements are in between these fields. The reconstruction and recognition needs to be done in less than half a second for customer comfort, while the reconstruction quality must be reliable for a dependable recognition.

Our multi-camera matching process consists of several nested loops as described in [5] and shown in Fig. 1 (right). This process is based on a system of four USB Logitech® cameras QuickCam® Pro 9000. These cameras run at a resolution of 960×720 at 5 fps connected via two USB 2.0

Controllers. Here, the USB-bandwidth limits the camera resolution. To get the best results we use a Y-constellation of the four cameras as shown in Fig. 1 (left). A camera constellation with a preferred direction could deteriorate the detection of features along this direction, e.g. horizontal stripes in the image cause problems in a horizontal camera constellation. Our method can be adapted to arbitrary camera constellations, independently of the used hardware system.

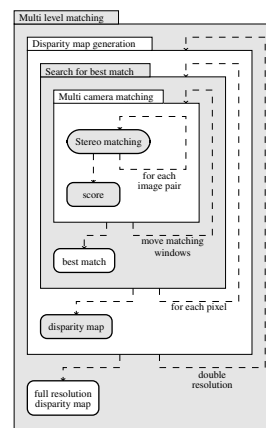


Figure 1: The matching process and the camera system.

Because our method mainly works on images and generates a depth map as an image, we use GLSL fragment shaders. For the complex shader operations GPUs which support at least shader model 4.0 are necessary.

The input data are multiple raw camera images. Each raw image is corrected by a shader implementing the lens correction. The resulting corrected images are rendered into separate textures. Each texture is then transformed into a mip-map (CIM) used by all subsequent shaders. Each step in our multi-level matching requires four fragment shader programs. The first shader takes the CIM and renders the weighted average color of the pixels of a matching window at the actual resolution level to separate average textures (AT). The second shader takes the CIM and the AT and renders the weighted auto-correlation for the same matching window to an auto-correlation texture (ACT). The third shader takes the AT and ACT and performs all matching operations, i.e. it moves the deformed matching windows, computes the total score, and finds the best sub-pixel score. The result is rendered as the disparity map (DM), the best total score of the finest resolution and the quality measure to the three color channels of a separate texture. The fourth shader takes the DM, smooths the disparities, and renders the result to a smoothed disparity map.



Figure 2: Sample images from our camera system.

Example images of our system are shown in Fig. 2. Fig. 3 shows the resulting texture holding the disparity map (red channel), the best total score of the finest resolution level (green channel), and the quality measure (blue channel).

After transformation of the disparities to real depth values, the data can be rendered as 3d model, see Fig. 3 (top right). Here, the low quality regions are masked and ignored.

The whole calculation for our example images at a resolution of 960×720 pixels takes an average GPU processing time of 7.5 ms on an NVidia GeForce GTX 285 GPU. Depending on the scene the average processing time can increase to 10.5

ms. This allows real-time frame rates of 95 fps. Our cameras capture only five fps of unsynchronized pictures. So we are not able to record 3d videos using this camera system.



Figure 3: Results: All color channels (top left), reconstructed 3d model (top right), disparity map (bottom left), quality measure (bottom right).

The quality of the resulting surface model is sufficient for our target application 3d face recognition. The processing times are more than sufficient for face recognition. Cameras with much higher resolution could allow for a better quality at still acceptable computation times. Additional methods like cross-checking or edge detection that can be implemented on the GPU could further improve our results. A camera system that can be synchronized would allow the recording of 3d video sequences.

Bibliography

- [1] D. Murray and J. Little. Using real-time stereo vision for mobile robot navigation. In *Autonomous Robots*, page 2000, 2000.
- [2] D.T. Pham and L.C. Hieu. Reverse engineering - hardware and software. In V. Raja and K.J. Fernandes, editors, *Reverse Engineering - An Industrial Perspective*, pages 33–30, 2008.
- [3] Y. Furukawa and J. Ponce. Accurate, dense, and robust multi-view stereopsis. In *CVPR*, 2007.
- [4] R. Yang, G. Welch, and G. Bishop. Real-time consensus-based scene reconstruction using commodity graphics hardware, 2002.
- [5] K. Denker and G. Umlauf. An accurate real-time multi-camera matching on the GPU for 3d reconstruction. In *Submitted to: ICCS 2010*.

Adaptive Tetrahedral Subdivision for Finite Element Analysis

Daniel Burkhart and Georg Umlauf



Realistic behavior of deformable objects is essential for many applications in computer graphics, engineering, or medicine. Typical techniques are either based on mass-spring-damper models, boundary element methods, finite difference methods, or finite element methods. These methods either lack accuracy or are computationally very expensive. If accuracy is required FEM computations use adaptive refinement, where regions with high gradients are refined locally. The bottleneck of this approach is still the gap between CAD and CAE representations.

We present an approach to utilize solid subdivision for finite element simulations using an adaptive tetrahedral subdivision scheme based on $\sqrt{3}$ subdivision for triangular meshes. The advantage of this approach is the use of the subdivision representation for the modeling, the visualization and the simulation of the solid model.

ODEs and PDEs arise in many computer graphics areas. Especially, physical simulation of deformable objects is essential for applications like computer animation, surgical training or mechanical engineering. While for surgical training real-time behavior is most critical, for mechanical engineering physically accurate behavior are preferred.

In this paper a method is presented using adaptive tetrahedral subdivision for finite element analysis. Utilizing a solid subdivision has many advantages: (i) one representation for modeling, visualization and simulation; (ii) implicit creation of high quality meshes; (iii) level of detail/adaptivity; (iv) special features; (v) efficiency/stability; (vi) simple rules/data structures; (vii) arbitrary topology.

Our adaptive tetrahedral subdivision scheme is designed for efficient computations of finite element analysis of models with sharp creases and corners as required in mechanical engineering. Furthermore, the boundary is a smooth subdivision surface. So, refinement does not require communication between the CAE- and the CAD-system, since new node positions are implicitly known.

The subdivision scheme for tetrahedral meshes we use for the FEM simulation generalizes the idea of $\sqrt{3}$ subdivision for triangular meshes, as it uses generalized split and flip operations [1]. Tetrahedral subdivision is based on tetrahedral 1-4 splits and multi-face removals (Fig. 1). The subdivision

process is a combination of 1-4 splits and 2-3 flips in the interior, the $\sqrt{3}$ scheme and edge removals on the boundary and optimization steps as shown in Fig. 2. For details see [1, 2].

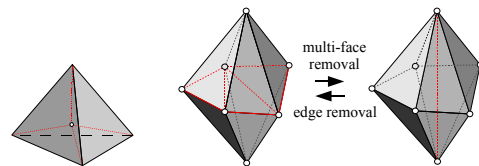


Figure 1: 1-4 split and multi-face removal.

In contrast to earlier solid subdivision schemes, this scheme allows for (a) adaptive refinement by restricting the 2-3 flips and the boundary edge removals to the locally refined regions, (b) control of the shape of the tetrahedra by adjusting the optimization steps, and (c) preservation of sharp features by adjusting the two smoothing operations. The latter can also be used to replace the original $\sqrt{3}$ smoothing by an interpolatory smoothing. These properties make this subdivision scheme suitable for FEM simulations.

Most research that has applied FEM in animation and simulation has used linear finite elements. To solve a continuum mechanical problem, the first step is to discretize the domain into a set of finite elements. However, the key to efficient and accurate solutions to these problems is not the quantity but also the quality of the elements. Thus, it is important to refine only in areas with large gradients,



Figure 2: The tetrahedral subdivision scheme (blue = interior, green = boundary).

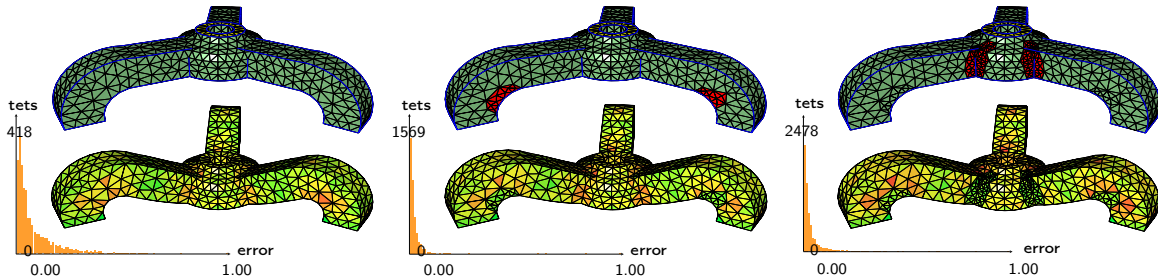


Figure 3: Two rounds of adaptive subdivision and FE simulation (top – bottom): tetrahedral base mesh (2,799 tetrahedra), simulation result with visualization of the normalized approximation error (green=low – red=high) and the histogram of the error distribution.

to keep the total number of elements small. This refinement requires adaptive meshing techniques, which must be combined with an appropriate error estimator, while at the same time the quality of the elements must be controlled. For this we use the tetrahedral subdivision scheme with optimization steps that maximize the minimal dihedral angles.

Our results were computed on a 2GHz Intel Core2 Duo with 4GB RAM using Getfem++ for the engineering part in Fig. 3 (left top) consisting of 2,799 tetrahedra. To the top faces (yellow) of the tripod a vertical load is applied, while the bottom of the legs of the tripod is fixed. Fig. 3 (left bottom) shows the deformed model. For the visualization of the normalized approximation error of the tetrahedra the color hue of the HSV model is linearly interpolated from 0° (low error) to 120° (high error). The simulation took 491ms while the average normalized error is 0.08. The histogram shows the error distribution for the tetrahedra.

For the next step the mesh regions with the largest error are refined, show in red in Fig. 3 (middle top). The adaptively refined mesh consists of 4,540 tetrahedra. Fig. 3 (middle bottom) shows the deformation of this new tetrahedral mesh. The simulation took 596ms while the average normalized error is 0.03. Fig. 3 (right) shows a second

step of adaptive subdivision and simulation. After the adaptive subdivision the mesh consists of 6,080 tetrahedra. The simulation took 606ms with an average normalized error of 0.01. Without adaptive refinement the mesh consists of 23,480 tetrahedra after one subdivision step. This yields a simulation time of 7,574ms with average normalized error 0.008 for the globally refined mesh. Note the decrease of the average normalized error and the histograms getting narrower.

The major advantage of this approach is that only one representation is used for modeling, visualization and simulation of solid models, by means of an adaptive tetrahedral subdivision tailored for FE applications. For the future we plan to combine this subdivision scheme with more complex FE models, e.g. non-linear deformations and subdivision refinable functions for the FE simulation.

Bibliography

- [1] D. Burkhart, B. Hamann, and G. Umlauf. Adaptive and feature-preserving subdivision for high-quality tetrahedral meshes. *CGF*, 29(1):117–127, 2010.
- [2] D. Burkhart, B. Hamann, and G. Umlauf. Adaptive tetrahedral subdivision for finite element analysis. *In: CGI*, 2010.

Optische Drehzahlmessung nach dem Korrelationsverfahren

Alexander Berk, Steffen Tschersch und Klaus Durst



Im Rahmen einer Projektarbeit [1] im Studiengang "Maschinenbau Konstruktion und Entwicklung" an der Hochschule Konstanz wurden grundlegende Experimente zur schlupffreien, berührungslos optischen low-cost-Drehzahlmessung nach dem Korrelationsverfahren durchgeführt, ein bestehender Labor-Prototyp [2] verbessert und mit LabVIEW eine automatische Auswertung der Drehzahl realisiert.

Üblicherweise wird die Geschwindigkeit von Kraftfahrzeugen über eine Drehzahlmessung bestimmt. Bei Schlupf, zum Beispiel auf glatten Fahrbahnen wie Schnee und Eis, bei Aquaplaning oder beim Eingriff des Antiblockiersystems, liefern Drehzahlmessungen keine brauchbaren Ergebnisse mehr. In diesen Grenzsituationen werden andere Messsysteme benötigt. Mit Hilfe der Kreuzkorrelation kann die Geschwindigkeit berührungslos und schlupffrei gemessen werden. Hier werden zwei optische Sensoren in einem definierten Abstand in Fahrtrichtung zueinander positioniert. Die beiden Sensoren liefern ein ähnliches Messsignal mit einem Zeitversatz. Die Geschwindigkeit lässt sich einfach berechnen, indem der Abstand der beiden Sensoren durch die Laufzeitdifferenz dividiert wird. Die Kreuzkorrelationsfunktion (KKF) hat die folgende allgemeine Form.

$$\phi(\tau) = K \int_{-\infty}^{+\infty} x(t) \cdot y(t + \tau) dt$$

Bei einer Drehbewegung mit der Umdrehungsdauer T werden periodische Signale miteinander korreliert und die KKF lautet:

$$\phi(\tau) = \frac{1}{2 \cdot T} \int_{-T}^{+T} x(t) \cdot y(t + \tau) dt$$

Die Abbildung 1 zeigt den Testaufbau mit einer drehbaren CD mit speziellem Aufdruck zur Simu-

lation verschiedener Fahrbahnbeläge. Die von den beiden optischen Sensoren aufgenommenen Signale werden durch OP-Verstärker aufbereitet, von einer simultan abtastenden Messwerterfassungskarte digitalisiert und im Rechner mit LabVIEW erfasst, bearbeitet und ausgewertet.

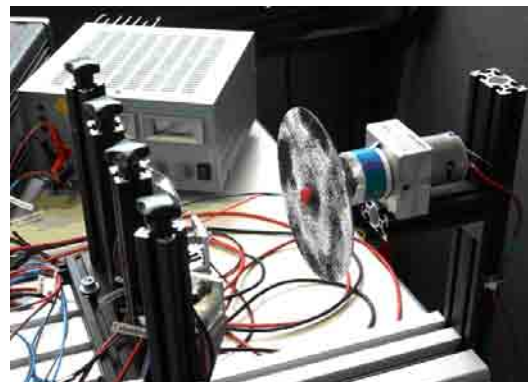


Figure 1: Versuchsaufbau

Die Erstellung des LabVIEW-Programmes für eine automatische Drehzahlbestimmung war Hauptbestandteil dieser Projektarbeit.

Das erstellte LabVIEW-Programm korreliert die beiden Signale miteinander, filtert die ausgegebenen Daten, wertet die Maxima bzw. Minima der KKF aus und rechnet anschließend die Differenzzeit in eine Drehzahl um. Innerhalb der Programmierung mit LabVIEW wird die KKF in der diskreten Form genutzt, da hier nur eine endliche Anzahl an Messwerten vorhanden ist.

Die Auswertung wurde in dieser Arbeit kontinuierlich zehnmal pro Sekunde durchgeführt. Aus der Abbildung 2 ist der LabVIEW-Auswertegraph mit den ermittelten Minima (hier durch grüne Punkte visualisiert) erkennbar.

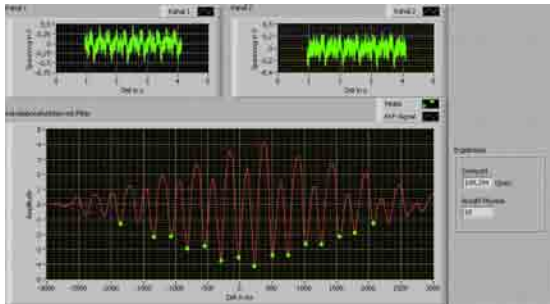


Figure 2: Messsignale der zwei optischen Sensoren (oben) und die gefilterte KKF mit ermittelten Minima (unten).

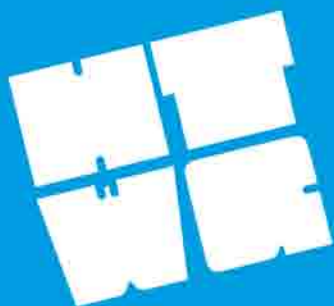
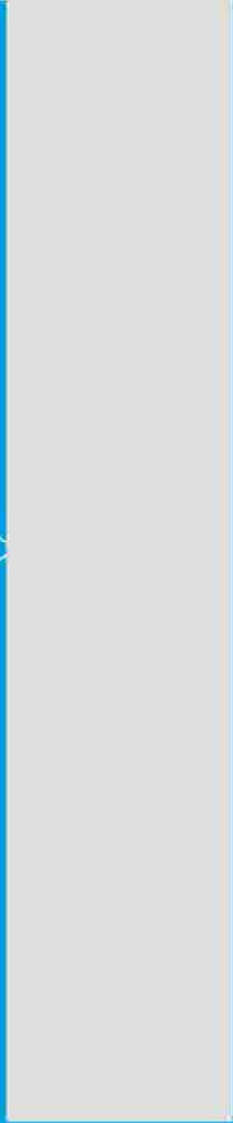
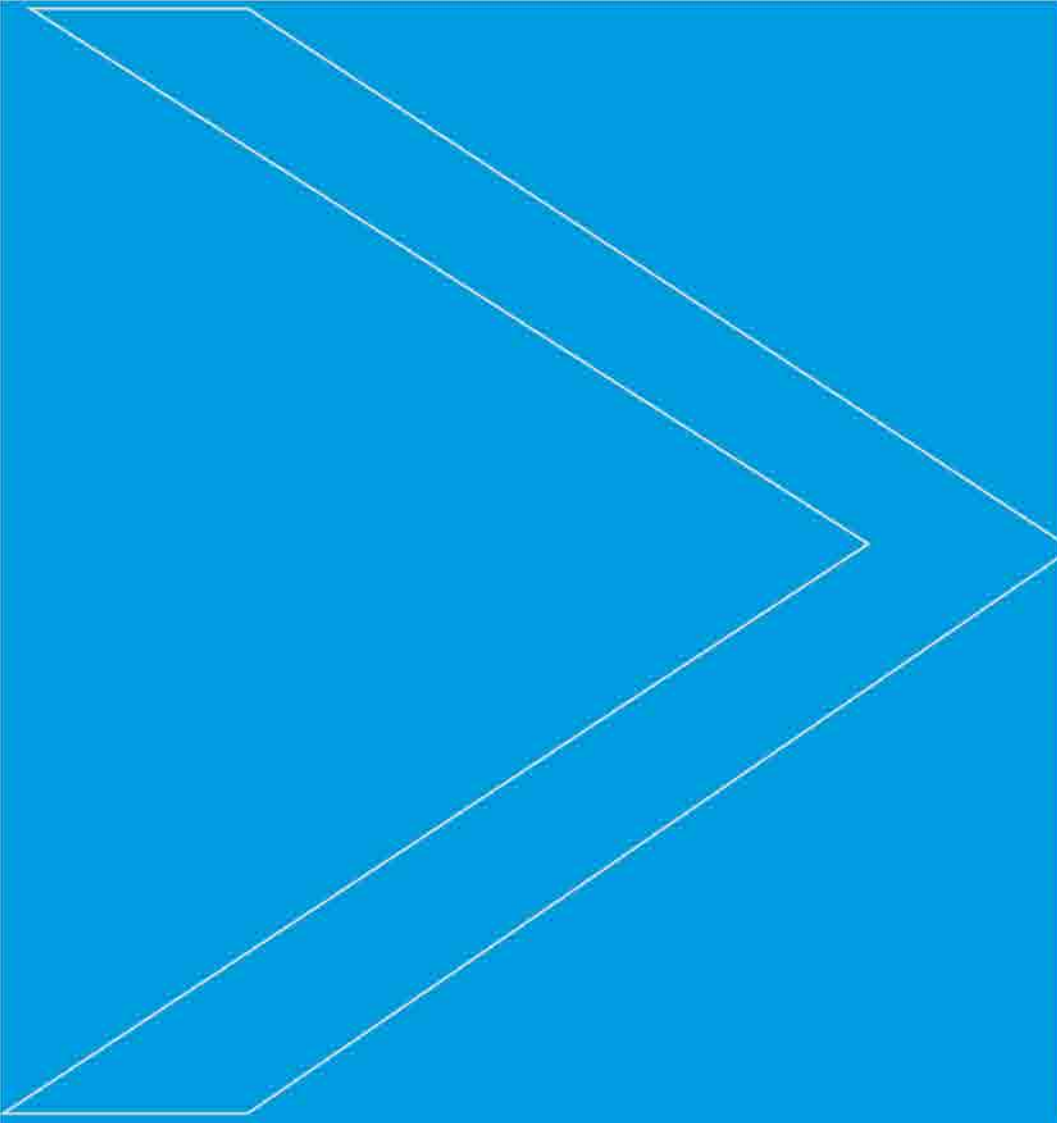
Mit diesem Graph und seiner Visualisierung der Maxima bzw. der Minima kann eine unmittelbare Einschätzung der Qualität der KKF-Ergebnisse und

der Drehzahlbestimmung vorgenommen werden.

Die gestellte Aufgabe einer robusten rechnergestützten automatischen Drehzahlbestimmung mit LabVIEW für die optische Drehzahlmessung nach dem KKF-Verfahren konnte in der vorliegenden Arbeit gelöst werden und es wurde gezeigt, dass eine zuverlässige optische KKF-Drehzahlmessung im low-cost-Bereich möglich ist.

Bibliography

- [1] A. Berk and S. Tschersch. Projektarbeit des Studiengangs Maschinenbau-Konstruktion und Entwicklung. Master's thesis, HTWG Konstanz, 2010.
- [2] K. Durst, A. Resch, and D. Merk. Zwischenbericht: Schlupffreie optische Geschwindigkeitsmessung nach dem Korrelationsverfahren. *Annual Report IOS Konstanz*, 2008.



institute for optical systems
